ABSTRACT

Title of Thesis: HEAT TRANSFER ANALYSIS FOR IMPROVED IN-SITU INFRARED TEMPERATURE DIAGNOSTICS IN MICROCOMBUSTORS

Ananthanarayanan Veeraragavan, Master of Science, 2006

Thesis Directed By: Professor Christopher P. Cadou, Department of Aerospace Engineering

This thesis investigates heat transfer processes occurring in microcombustors. First, a simple 2D model is developed for predicting temperature profiles in a premixed laminar flame propagating between two parallel plates. The model is used to generate a correlation for the variation in Nusselt number with downstream distance which is useful for numerical simulations. It also shows that the temperature profile across the channel is well approximated using either 2^{nd} or 4^{th} order polynomials. Second, the functional form of the gas temperature profile is used to demonstrate a new diagnostic technique for making non-intrusive measurements of gas temperature and wall heat fluxes. The technique is applied in a silicon-walled microcombustor (5 cm x 2 mm x 5.5 cm). The gas temperature and wall heat flux measurements are combined with measurements of the wall temperature distribution to develop a complete picture of heat transfer in the microcombustor. The results show that thermal feedback from the post-flame to the pre-flame via the structure is the dominant heat transfer path in microcombustors.

HEAT TRANSFER ANALYSIS FOR IMPROVED IN-SITU INFRARED TEMPERATURE DIAGNOSTICS IN MICROCOMBUSTORS

by

Ananthanarayanan Veeraragavan

Thesis submitted to the Faculty of the Graduate School of the
University of Maryland, College Park, in partial fulfillment
of the requirements for the degree of
Master of Science
[2006]

Advisory Committee:

Professor [Chrisptoper Cadou] Chair
[Professor Kenneth Yu]
[Professor Peter Sunderland]

Acknowledgements

I would like to take this opportunity to thank my advisor Prof. Chris Cadou for his guidance over the entire course of my Master's work. He has been a prime motivator and firm believer in my ability to do well and quite frankly more than half of all my research would never have attained the final form and niceness it now has but for his vision and his pushing me to do better than what I can. I would also like to thank my advisory committee Prof.'s Ken Yu and Peter Sunderland; both of whom have always been open and approachable at any time.

I would also like to thank all my comrades at UMD: Scott, Shyam, Ritesh, Gaby, Kiran and Tim, my relationship with all of whom has not just been that of a co-worker but of a true friend and a well wisher. Thank you for all the laughs and the serious discussions most of which has reflected in whom I have evolved to become over the past 3 years.

I would like to acknowledge the love and support of my dear sister Bhuvana, whose patience and endearance (even if only over the telephone for the past 3 years) has been a key aspect of my achieving what I have. I would also like to thank my parents (Mr. A. Veeraragavan and Mrs. R. Lakxshmi), my uncle Mr. Ganesh Shastri, my aunt Mrs. Jaya Shastri, my aunt Mrs. Shanta Venkatachalam and all my cousins and my grandparents and all other members of my family for their support and blessings.

I take this chance to also say 'thank you for being there' to my friends for life: Sub, Baa, Dilip, Bala, Subash and Shravan all of whom are integral parts of my past and shall always remain in my heart.

Last but not the least I would like to express my sincere thanks to Dr. Mitat Birkan and the Office of Naval Resarch for their support and funding for this work.

Table of Contents

List of Tables

List of Figures

Chapter 1: Introduction

1.1 Motivation

1.1.1. Micro-scale combustion enables improved power systems:

Study of combustion at the micro scale (i.e., in passages with channel dimensions <3mm) has become important recently because of the fact that hydrocarbon fuels can store fifty to one hundred times (~50-100 MJ/Kg) the energy of a battery (~1 MJ/Kg for a Li-Ion battery) of similar weight. This has sparked a great interest in devising efficient ways for releasing this energy and converting it to electrical power in a compact system. In order for these systems to be practical however, they need to be at least 1 % efficient in order to match the performance of batteries and 10-20 % efficient to increase life span or power output by factors of 10-20.

There are many applications of micro-combustion devices in addition to battery replacement. Two of the most important are propulsion systems for nano and pico satellites (0.1 – 10 Kg range) and for micro aero vehicles (MAV).

1.1.2. New diagnostic techniques required for microcombustion

The advance of combustion science depends on the ability to make measurements which can be compared to analytical and numerical models.

Accordingly, many diagnostic tools have been developed to make temperature and species concentration measurements in combustors. These include physical probes like thermocouples[1], exhaust gas analyzers[2], and non-intrusive techniques

(like absorbance/transmission spectroscopy[3-6]). These techniques have been used with great success in conventional combustors where the probes and measurement volumes are much smaller than the characteristic length scale of the combustor. When the device is scaled down, however, the measurement volumes are much smaller than the characteristic length scale of the combustor. The smaller volumes coupled with the high temperatures and oxidizing environment inside the combustor make it difficult to use intrusive methods like thermocouples or gas sampling probes. Therefore non-intrusive diagnostics are required. While there has been considerable work focused on developing non-intrusive measurement techniques for microscale devices most have focused on velocity measurements and none has considered reacting flow.

1.2 Challenges in Microcombustion

In this thesis microcombustion is defined as combustion in passages with characteristic dimension of the order of/or less than the reaction zone thickness. Microcombustion has several key differences compared to combustion at the conventional scale because as the size of the device reduces the ratio of surface area to volume increases. The first is that combustors get less efficient as their size is reduced. This is because most of the loss mechanisms (i.e., friction, convective and radiative heat transfer) are proportional to the surface area while the energy release is proportional to volume. Therefore, reducing the size of the device increases the surface to volume ratio thereby increasing the relative importance of the losses and reducing overall efficiency. The second is that as the combustor is scaled down, its structure becomes more involved in the flame stabilization process. The net effect is

highly variable as axial heat transfer through the structure can act as a stabilizing mechanism, whereas radical quenching at the surface and heat loss to the environment may quench reaction.

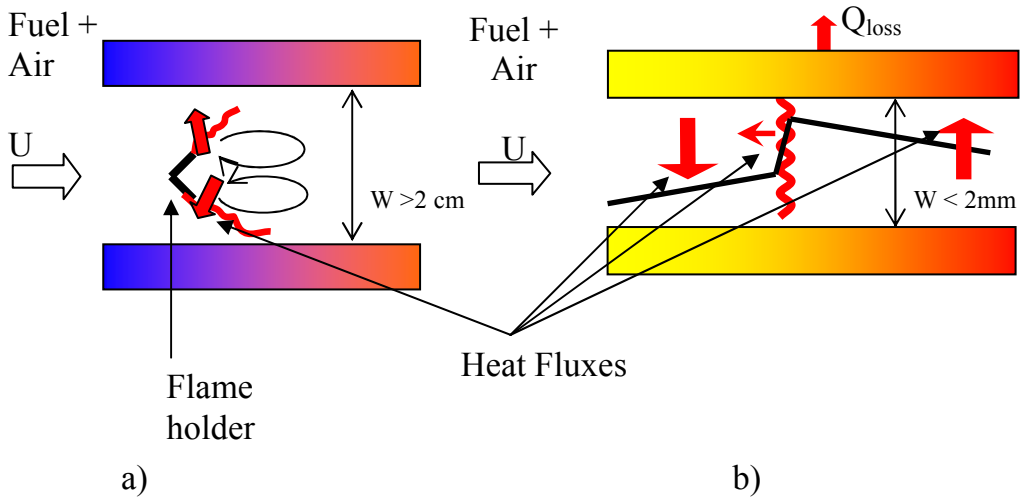

Figure 1-1: Illustration of flame holding in combustors; a) Conventional Scale, b) Microscale

Fig. 1-1 is a simple illustration of the difference between flame holding mechanisms in conventional and microscale combustors. In the flameholder, hot combustion products are recirculated upstream to ignite reactants. In microcombustors, heat transfers upstream via structure to ignite reactants. In addition heat loss to the environment in microscale combustors will much more significant than that in conventional scale combustors because the walls are in stronger thermal contact with the hot products and so will heat up more.

1.3 Relevant Previous Work

1.3.1. Micro-combustion research

Early studies of combustion in small passages focused on the importance of heat loss and chemical quenching on flame propagation and extinction. Zeldovich[7] showed that there was a minimum radius for tubes below which premixed flames were unable to propagate and got quenched. Recently attention has shifted to combustion in micro-channels. Daou and Matalon[8] studied the interaction between the effects of velocity, heat loss to the structure, and passage width on premixed flames in channels with an allowance for heat exchange with the environment. The result of their work was an extinction map for flames in channels that showed that heat losses to the walls could partially or completely extinguish the flame. Ronney[9] developed a 1-D model of a heat recirculating burner, and showed that heat conduction within the structure is the dominant process governing flame stabilization. Further evidence of the dominance by the structure is given by Cui *et al.* [10], who have shown that the behavior of flames stabilized in meso/microscale channels no longer depends on the Lewis number. Work by Leach[11] *et al.* has also shown that axial conduction of heat through walls plays a major role in determining micro-combustor performance. Using a simple 1-D model of a flame held between two infinitely long plates, Leach and Cadou[12] showed that axial conduction through the structure and distributed heat transfer between gas and structure causes the reaction zone to broaden and the burning velocity to increase.

Many of the conclusions regarding flame stabilization in microcombustors are similar to those reached in the late 1970's and early 1980's by researchers like

Takeno[13-15] who studied "excess enthalpy flames". They demonstrated theoretically and experimentally that heat recirculation through a combustor's structure (in this case a porous medium or a packed bed) played an important role in flame stabilization. Excess enthalpy flames were also studied extensively by Weinberg, a good account of which can be found in his text book[16].

The recent interest in the physics of microscale combustion has been driven in large part by efforts to develop a microscale heat engine that consumes liquid hydrocarbon fuels in a miniature combustor with dimensions below 1mm.

The first such effort was by MIT which seeks to develop a Micro-Electro-Mechanical Systems (MEMS) micro gas turbine[17] with an integral electrical generator intended to produce 10-50W of power. The over all size of the device is about 2.1 cm x 2.1 cm x 0.38 cm. The device is silicon based and is constructed by bonding six individual silicon wafers to form the compressor, turbine, combustor, generator and other flow passages. While the components of the proposed engine have been operated independently a complete device has not been operated yet.

Fernandez-Pello[18] and co-workers are developing a micro-rotary engine intended to produce ~10-100 mW of power. The mini-rotary fabricated using electrodischarge machining (EDM), has a displacement of 0.064 mm^3 and a rotor of size 1mm. The rotary design simplifies the design significantly as it eliminates the need for valves. A key aspect of developing any microscale engine is to avoid unnecessary moving parts, sealing or lubrication issues if possible. Higher complexity brings with it a greater risk of failure.

Kittelson's[19, 20] and coworkers are developing a homogenous charge compression ignition (HCCI) micro-engine capable of producing 10W. HCCI engines differ from conventional compression and spark ignition engines in that these compress premixed fuel and air until it ignites spontaneously. This enables operation at very low overall equivalence ratio which can reduce NO_x. It also eliminates the need (in theory at least) of an external ignition system. This makes the design less complex. In the design, combustion drives a free piston design which serves as the moving element in a permanent magnet generator.

Ronney *et al.* [21, 22] have built heat recirculating burners for use with thermoelectric generators. The burners are a 'Swiss roll' design and work by allowing heat to be exchanged between product and reactant streams. The counter-current heat exchanger design greatly reduces heat loss to the environment, as most of the surface is exposed to cool reactants and most of the heat goes to preheating rather than being lost to the environment. Heat recirculation also widens the flammability limits of the burner by preheating the incoming reactants. While thermoelectric materials are relatively inefficient in converting heat to electric power, the Swiss roll design has the advantage of high thermal efficiency without the need for moving parts.

Dahm[23] and coworkers are developing an oscillatory rotating free-piston engine called MICSE for Micro Internal Combustion Swing Engine. The engine is intended to produce about 20 W with an overall efficiency of 14 %. Butane is the fuel and the engine is fabricated from steel using wire EDM. The diameter of the swing arm is 16 mm.

A bi-propellant micro-thruster was developed by London[18] at MIT that was based on the combustion of O_2 and CH_4. In spite of the device's small size, viscous losses did not prevent the generation of about 1 N thrust at a chamber pressure of 12 atmospheres.

1.3.2. Heat transfer in micro-channels

An alternate view of the microcombustion problem is one based on heat transfer in a duct flow with a combustion wave in it. This segregates the physical process of heat transfer from other intricate chemical properties of reacting flows in small scales. Earlier heat transfer analysis in ducts can be traced back to the classical paper by Graetz[25] where he developed an analysis that resulted in an expression for the Nusselt number (heat transfer number) as a function of the streamwise coordinate. However, Graetz's formulation did not account for the axial conduction of heat through the gas. This was probably because he was developing solutions for heat exchanger configurations; where most of the heat transfer occurs between the gas flow and the wall in a direction perpendicular to the flow direction. The classical theory for flame propagation however relies entirely on axial conduction of heat in the streamwise direction. This is because in conventional scales the incoming reactants get heated up predominantly due to heat transfer in the axial direction via thermal conduction in the gas. Sellars et al.[26] extended Graetz's work in this area to account for a variety of boundary conditions (constant wall temperature, prescribed wall temperature, and prescribed wall heat flux etc.) for both rectangular and circular ducts. Axial conduction through the gas was still not included. Other investigations have been undertaken to obtain Nusselt number relations for various duct geometries

with different boundary conditions. Analyses by Ebadian and Zhang[27], Michelsen and Villadsen[28], Telles et al.[29], Lahjomri and Oubarra[30] all focus on solving the extended Graetzian problem with axial heat conduction (in the gas) for various wall boundary conditions. The applications were for heat exchangers at either the conventional scale or microscale. A good summary of the work done in this area is given in the book by Kakac[31].

The heat transfer discussed so far focused on heat exchangers and imposed thermal boundary conditions at the wall in order to obtain solutions. In many cases however, heat transfer between the fluid and wall along with heat transfer within the structure of the wall itself are important. Jarosinksi[32] analyzed heat transfer between hot combustion products and cold wall in 'limit flames' by developing an analytical model. The author defined 'limit flames' as those that are close to being extinguished via excessive heat loss to the wall. The heat transfer between the wall and the fluid was modeled by means of a convective transport term (much like Leach et al.[12]). One of the chief results was the development of a relationship between the Nusselt number and the heat transfer Peclet number for post combustion heat exchange between hot combustion products and the cold wall for a 'slug' flow (see Chapter 3 for a simple model based on *Pe* number). This analysis was pseudo-2D as the heat transfer between the gas and the wall was still modeled based on a convective heat transfer coefficient and thus did not fully capture the complete physics of the problem.

Yin and Bau[33] developed analytical models for heat exchange in small ducts and channels with 1-D (slug) and 2-D (Poiseulle) flows. Their models incorporated heat loss to the wall and used eigen function expansions to relate the Nusselt number

to the Peclet number and the stream wise coordinate in micro heat exchangers. More recently Maranzana et al.[34] performed extensive analyses of heat transfer in micro and mini heat exchangers with passage heights of the order of 10 μm to a few mm. They included heat transport via the structure of the heat exchanger and introduced a new non-dimensional number M to indicate the relative function of conductive axial heat transfer in walls in order to emphasize the importance of axial heat transfer through the walls in small scale heat exchangers.

Since microcombustors need to be as small as possible, the flow within them will probably not be fully developed (thermally and or hydrodynamically) and entrance effects are expected to be important. Hsu[35] studied a complex entrance effect problem which accounted for both the transverse non-uniformity in the velocity field and axial conduction in the gas. Sucec and Radley[36] studied unsteady heat transfer in a hydrodynamically fully developed duct flow where the wall temperature is impulsively changed to a prescribed profile. The governing equations were solved using Laplace transformations. Their conclusion was that when such sudden variations are encountered, approximating the physics using steady state conditions yields appreciable errors in heat flux calculations. In 1992 Silva et al.[37] investigated the simultaneous development of 2-D temperature and velocity profiles in a channel formed between two infinitely long parallel plates. They adopted a linearization procedure for the velocity and thus decoupled the energy equation and solved it using integral transforms. More recent studies (Nield et al.[38]) have focused on thermally developing flow in porous media. The common thread in all of these studies is that they start with the classical Graetzian problem and then adapt themselves for the

particular problem of interest. The modern day extensions to the Graetz problem also usually account for axial conduction in gas and transverse variations in velocity and temperature.

1.3.3. Measurement techniques and diagnostics:

1.3.3. a) Conventional Scale:

A variety of non-intrusive methods are available for measuring temperature, composition (species concentration) and velocity fields in conventional scale systems.

Particle Image Velocimetry (PIV) is a flow visualization technique in which the flow is seeded with particles which are illuminated by a laser sheet. Images of the particles at different times are captured using a fast CCD camera and the velocity field is determined by computing the auto course[39].

Transmission Fourier transform infrared (FTIR) spectroscopy is often used to make non-intrusive measurements of species concentrations and temperature. It involves passing a beam of light through the sample and measuring molecular absorption as a function of wavenumber using a detector that records the number of photons exiting the sample volume for each wavenumber. In contrast, emission FTIR spectroscopy collects photons that are naturally emitted by the sample. Emission FTIR is often used in combustion measurements since the high temperatures of the combustion environment excite vibrational transitions of most molecules leading to relatively strong emissions that are easy to collect. Emission experiments have the advantage that there is no beam to send through the sample to be collected by a detector. This makes the setup much less complicated, reducing the number of optical components required, and eliminates problems with beam steering. Also, this

allows remote sensing measurements of radiative sources at a distance. Jaquot et al.[3] measured temperatures of hot combustion exhaust gases using emission spectroscopy. They used the EM2C narrow band model to infer gas temperature from CO_2 spectra. Measurements of temperatures up to 1100 K have also been made. Bailly et al.[4] used a high resolution spectrometer (0.02 cm^{-1}) to infer gas temperature from CO_2 spectra by only considering the transitions that are excited at high temperatures. The temperatures were obtained with precisions on the order of ±1% for this method.

Transmission FTIR is the most common form of FTIR spectroscopy because the sample does not have to be at the high temperatures needed for emission measurements. In this technique, a beam is sent through the sample and the molecules absorb light. One particularly relevant investigation to the work presented here is that of Lindner and co-workers[5] who used FTIR measurements to infer gas temperature, CO_2 concentration and combustion efficiency. They used an in-house wide band model with constants obtained from the literature to compute gas temperature and concentrations. Both emission and absorbance measurements were used in this experiment. Koshland et al.[6] used in situ transmission FTIR to detect chlorinated hydrocarbons in combustion flows. Modest et al.[40] compared the predictions of Hitran[41], Hitemp[42], Radcal[43], and EM2C[44] using an isothermal drop-tube burner and transmission spectroscopy. Their results indicated that the wide band models (Radcal and EM2C) are better able to predict the band structure at higher temperatures (i.e., > 1300K) with EM2C being slightly better than Radcal in this respect.

1.3.3. b) Microscale:

The combination of small volumes and the presence of high temperatures, oxidizing environment and the difficulty of providing appropriate optical access have prevented the use of most conventional combustion diagnostic tools at the microscale. As a result, there are relatively fewer examples for such diagnostic tools in the microscale. Zhang and co-workers[45] developed miniature thermocouples that are micro-fabricated into the combustors structure. While they could be useful in low temperature reacting flows found in catalytic systems, they are unable to survive at temperatures associated with most gas phase combustion processes. Breuer[42] has taken advantage of silicon's transmissivity in the infrared regime to measure velocity using Micro-Particle Image Velocimetry (MPIV). Breuer's technique uses volume illumination and narrow depth of field camera optics to eliminate the need to produce a sheet of light with thickness of a few microns.

Heatwole et al.[47] demonstrated the feasibility of using silicon's transmissivity in the IR to make absorption measurements using FTIR spectroscopy. Concentrations of CO, CO_2 and CH_4 were determined from the integrated absorbance of each molecules rotational band. Gas temperature was determined from measurements of rotational line strengths and comparison to predictions of the HITRAN database. Unfortunately, however, the uncertainties in the individual line strengths in the HITRAN database led to unacceptably large uncertainties in temperature.

1.4. Objective and approach:

The objectives of this thesis are to improve the non-intrusive gas temperature measurement method developed by Heatwole et al.[47] so that it has a useful level of

uncertainty (± 200 K) and to use the technique to measure the heat fluxes in a simulated microcombustors. This will required extending the technique to incorporate the variation of the temperature along the beam path and determining the functional form of the variation in gas temperature across the channel in a direction perpendicular to the gas flow. The functional form of the temperature profile will be determined using a simple, two dimensional heat transfer model. Once the functional form of the temperature profile is known, this profile may be adjusted to provide the best fit to the data and the differentiated to determine the heat flux at the wall. Finally, the gas temperature and heat flux measurements will be combined with surface temperature measurements to construct a complete picture of the heat transfer occurring in a microcombustor.

Chapter 2: Heat Transfer Model for a Microcombustor

2.1. Description of Problem Domain:

The starting point for this analysis is the schematic diagram of the simple micro-scale combustor illustrated in Fig. 2-1. It consists of two parallel plates separated by a distance 2d and a plenum from which pre-mixed fuel and air enter the flow channel. The origin for the model problem is located at the flame front and the flame is assumed to be far enough downstream in the channel that the plenum does not need to be considered.

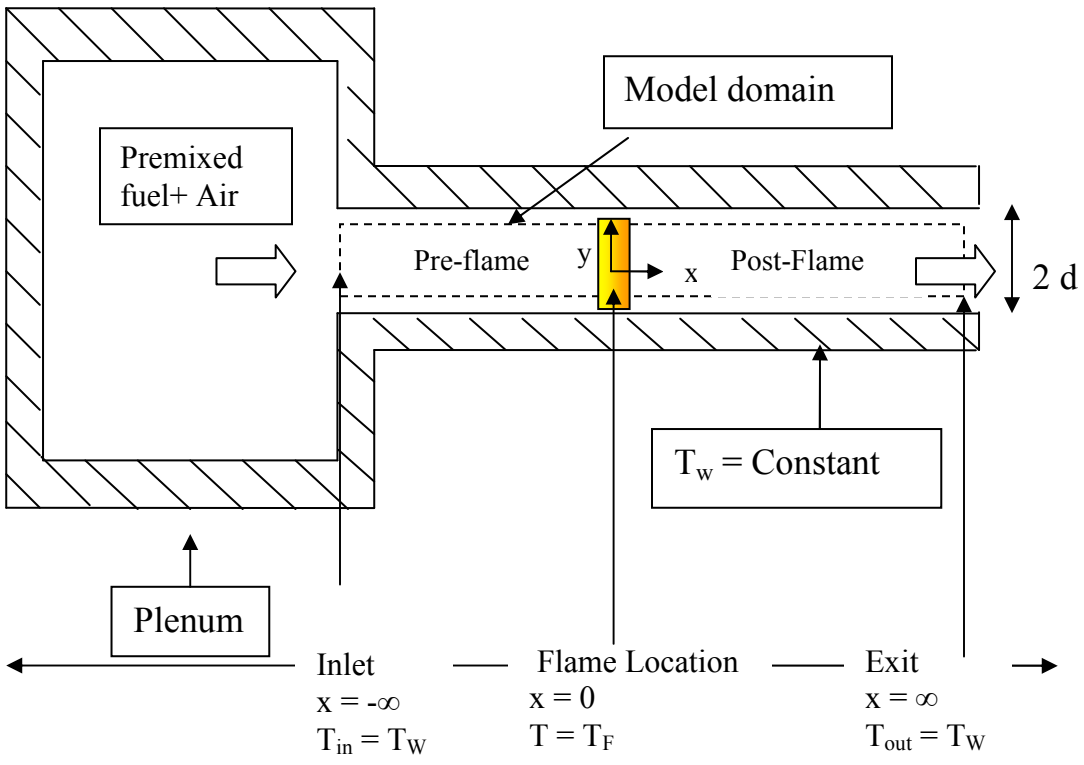

Figure 2-1: Schematic sketch of the model adopted (slot cross section)

The boundary conditions are prescribed in the form of temperature values at the ends of the pre and post flame regions. For the pre-flame region this consists of an inlet temperature (equal to the temperature of the plenum which equals the wall temperature T_W) and an ignition temperature (just as combustion begins) at the flame front ($x = 0$). For this purpose of this analysis, the ignition temperature is assumed to be close to the adiabatic flame temperature T_F. The boundary conditions for the post flame region are that the gas temperature equals the ignition temperature at the left end (flame front) and that the gas temperature equals the wall temperature at the far right end (after losing all the excess heat to the wall

2.2. Mathematical Formulation and Non-dimensionalization:

Conservation of energy in the gas flow is given by:

$$\rho U Cp \frac{\partial T}{\partial x} = k\left(\frac{\partial^2 T}{\partial x^2} + \frac{\partial^2 T}{\partial y^2}\right) + \dot{\omega}_F h_R \tag{2-1}$$

with boundary conditions

$$\begin{aligned} &T(-\infty, y) = T_W; \\ &T(0, y^+) = T_F; \quad \text{and} \quad \left.\frac{\partial T}{\partial y}\right|_{y=0} = 0 \quad \& \quad T(x, d) = T_W; \\ &T(\infty, y^+) = T_W; \end{aligned} \tag{2-2}$$

Slug flow is assumed (i.e., the flow velocity U is assumed to be constant across the channel). Since the flame is assumed to be thin (i.e., a flame sheet), when we solve Eq. 2-1 we neglect the reaction term in the pre-flame and post-flame regions. The boundary conditions in the lateral (perpendicular to the streamwise) direction arise because the wall temperature is prescribed to be constant and that the geometry of the channel makes the flow symmetric about the centerline.

Eq. 2-1 is non-dimensionalized as follows. A non-dimensional temperature is defined as:

$$\theta = (T - T_W)/ (T_F - T_W) \tag{2-3}$$

In this expression, T_W is the wall temperature, and T_F is the adiabatic flame temperature. Non-dimensional spatial coordinates are defined as

$$x^+ = x/d \text{ and } y^+ = y/d \tag{2-4}$$

where d is the channel half width. Other non-dimensional parameters are the Peclet number (Pe), the Reynolds number (Re) and the Prandtl number (Pr) defined as

$$Pe = Re\ Pr = (Ud/\nu)\ (\nu/\alpha) = (U\ d\ Cp\ \rho) / k \tag{2-5}$$

This leads to the following non-dimensional energy equation for the pre-flame and post-flame regions (where the reaction rate is taken to be zero). Thus conservation of energy is expressed as a single equation that depends on the two spatial variables and just one non-dimensional number (Peclet number).

$$Pe\frac{\partial\theta}{\partial x^+} = \frac{\partial^2\theta}{\partial x^{+2}} + \frac{\partial^2\theta}{\partial y^{+2}} \tag{2-6}$$

The transformed boundary conditions become:

$$\begin{aligned} &\theta(-\infty, y^+) = 0; \\ &\theta(0, y^+) = 1; \quad \text{and} \quad \left.\frac{\partial\theta}{\partial y^+}\right|_{y^+=0} = 0 \quad \& \quad \theta(x^+, 1) = 0; \\ &\theta(\infty, y^+) = 0; \end{aligned} \tag{2-7}$$

2.3. Solutions:

2.3.1. General Solution:

Eq. 2-6 is solved using separation of variables by writing the non-dimensional temperature as a product of two functions that depend only one either one of the spatial variables as below.

$$\theta(x^+, y^+) = X(x^+)\, Y(y^+) \tag{2-8}$$

Substituting Eq. 2-8 into Eq. 2-6 and applying boundary conditions (Eq. 2-7) leads to eigenfunction solutions of the form.

$$\theta(\mathrm{x}^+_{\text{pre-flame}}, y^+) = \sum_{n=0}^{\infty} A_n \exp\left(\frac{Pe + \sqrt{Pe^2 + 4\lambda_n^2}}{2}\, \mathrm{x}^+_{\text{pre-flame}}\right) \cos(\lambda_n\, y^+) \tag{2-9}$$

$$\theta(\mathrm{x}^+_{\text{post-flame}}, y^+) = \sum_{n=0}^{\infty} B_n \exp\left(\frac{Pe - \sqrt{Pe^2 + 4\lambda_n^2}}{2}\, \mathrm{x}^+_{\text{post-flame}}\right) \cos(\lambda_n\, y^+) \tag{2-10}$$

With the eigenvalue given by[†]

$$\lambda_n = (2n + 1)\pi/2 \tag{2-11}$$

Matalon[8] has obtained solutions that are similar in nature (i.e. the exponential terms in the pre-flame and post-flame regions) using an asymptotic expansion. Maruta[48] et al have also found similar exponential solutions for combustion in heated micro-channels. They solved the combustion characteristics for time dependent, 1D energy equation for flame propagation in a parallel plate configuration. The simple 2D model adopted here manages to capture the same physics in terms of the exponential form of the solution in the pre-flame and post-flame regions. The solutions (Eqs. 2-6 and 2-7) approach zero as $x^+ \rightarrow \pm\infty$ for the two regions and when

[†] The details of the solution are presented in the appendix

y^+ equals 1. The constants A_n and B_n are evaluated using the boundary condition at the flame front ($x^+ = 0$) which requires that the non-dimensional temperature θ equal 1, and by noting that the summation series is expressed in an orthogonal basis.

$$A_n = B_n = 2\int_0^1 \cos(\lambda_n y^+)dy = 2\frac{(-1)^n}{\lambda_n} \tag{2-12}$$

Therefore, the entire solution in the pre and post-flame regions can be expressed as an infinite sum that depends only on the Peclet number and the eigenvalues (λ_n). This is consistent with previous 1-D solutions for *freely propagating flames*[49] where heat conduction in the lateral direction is neglected and the energy equation is expressed as a balance between convective transport in the axial direction and heat conduction in the axial direction. The solution for this 1D situation is[‡]:

$$\theta = \begin{cases} \exp(Pe\, x^+); & x^+ < 0 \quad (pre-flame) \\ 1; & x^+ \geq 0 \quad (post-flame) \end{cases} \tag{2-13}$$

for the pre-flame and θ= const (ie. constant gas temperature) after the combustion wave.

In order to compare our 2D solution with Williams's[49] 1D analysis we compute the mean value of θ across the channel.

$$\begin{aligned} \theta_m &= \int_0^1 \theta(x^+, y^+)\, dy^+ \\ &= \int_0^1 \sum_{n=0}^{\infty} 2\frac{(-1)^n}{\lambda_n} \exp\left(\frac{Pe \pm \left(Pe^2 + 4\lambda_n^2\right)^{1/2}}{2} x^+\right) \cos(\lambda_n y^+)\, dy^+ \end{aligned}$$

[‡] The solution presented in the reference has been non-dimensionalzied according to the convention adopted in the analysis here and presented to enable direct comparisons.

This gives the following 1-D expressions for the temperature as a function of axial coordinate in the pre-flame and post-flame regions that are suitable for comparison with Williams' solution that does not include the effect of transverse conduction.

$$\theta_m = \begin{cases} \sum_{n=0}^{\infty} \frac{2}{\lambda_n^2} \exp\left(\frac{Pe + \sqrt{Pe^2 + 4\lambda_n^2}}{2} x^+\right); \; x^+ < 0 \quad (pre-flame) \\ \sum_{n=0}^{\infty} \frac{2}{\lambda_n^2} \exp\left(\frac{Pe - \sqrt{Pe^2 + 4\lambda_n^2}}{2} x^+\right); \; x^+ \geq 0 \quad (post-flame) \end{cases} \tag{2-14}$$

2.4. Large *Pe* number case:

Fig. 2-2 compares non-dimensional axial temperature profiles for the two and three-dimensional situations for three values of the Peclet number.

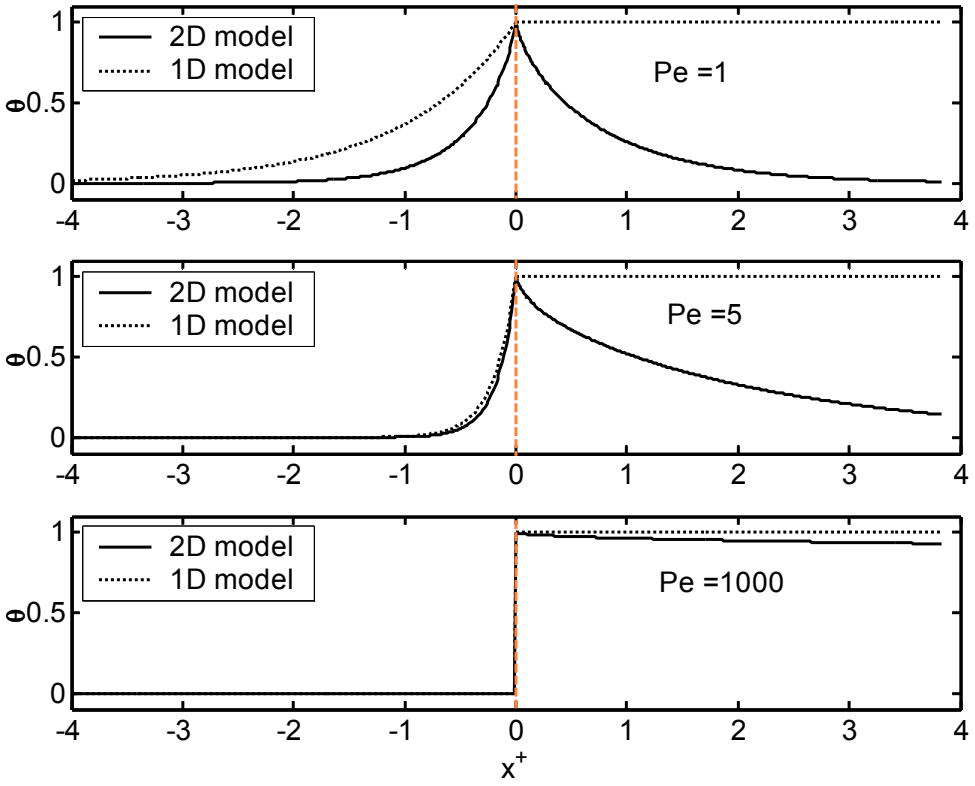

Figure 2-2: Plot of mean temperature (2D and 1D) for different *Pe* numbers

The figure shows that when the Peclet number is small, heat transfer in the transverse direction is strong and causes the gas temperature to fall rapidly downstream of the reaction zone. Therefore, two-dimensional effects are important when the Peclet number is small. Conversely, the mean temperature profile for the 2D case approaches the 1D solution when the Peclet number is large. This can be shown explicitly by re-writing Eq. 2-14 as follows

$$\theta_m = \begin{cases} \exp(\frac{Pe\, x^+}{2}) \sum_{n=0}^{\infty} \frac{2}{\lambda_n^2} \exp(\frac{\left(1+\frac{4\lambda_n^2}{Pe^2}\right)^{1/2}}{2} Pe\, x^+); \quad x^+ < 0 \quad (pre-flame) \\ \exp(\frac{Pe\, x^+}{2}) \sum_{n=0}^{\infty} \frac{2}{\lambda_n^2} \exp(-\frac{\left(1+\frac{4\lambda_n^2}{Pe^2}\right)^{1/2}}{2} Pe\, x^+); \quad x^+ \geq 0 \quad (post-flame) \end{cases} \tag{2-15}$$

and taking the limit as the Peclet number being large. When *Pe* number is very large, Eq. 2-15 becomes:

$$\theta_m = \begin{cases} \exp(Pe\, x^+) \sum_{n=0}^{\infty} \frac{2}{\lambda_n^2}; \quad x^+ < 0 \quad (pre-flame) \\ \sum_{n=0}^{\infty} \frac{2}{\lambda_n^2}; \quad x^+ \geq 0 \quad (post-flame) \end{cases} \tag{2-16}$$

From Eq. 2-11 we find that

$$\sum_{n=0}^{\infty} \frac{2}{\lambda_n^2} = \frac{8}{\pi^2} \sum_{n=0}^{\infty} \frac{1}{(2n+1)^2} = \frac{8}{\pi^2} \times \frac{\pi^2}{8} = 1 \tag{2-17}$$

where the summation series has been evaluated using the Parseval's equality condition[50] on the Fourier sine series expansion of unity on the interval [0, π]. Substituting Eq. 2-17 into Eq. 2-16 gives

$$\theta_m = \begin{cases} \exp(Pe\, x^+); \quad x^+ < 0 \quad (pre-flame) \\ 1; \quad x^+ \geq 0 \quad (post-flame) \end{cases} \tag{2-18}$$

Therefore, the solutions for the 1D and 2D cases are identical in the limit of large *Pe* number.

This result can also be used to explain the differences between micro-scale and conventional-scale combustors. Since *Pe* number is directly proportional to the channel width and the flow velocity, one could also say that the 2D case is well approximated by the 1D result when the passage height and flow velocity are relatively large (as in a conventional-scale combustor). What this means physically is that in the case of a large combustor, any thermal interaction between the wall and the gas is quite localized and the bulk of the gas does not sense this interaction. Alternatively, if the flow velocity is very large, the time for thermal interaction between the gas and the wall is much reduced (at each and every location) resulting in the gas phase "not seeing" the wall and behaving like an adiabatic 1D flow. These results confirm that wall interactions will be important in micro-scale combustors and must be accounted for.

2.5. Small *Pe* number case:

A similar analysis is performed for the situation where the Peclet number tends toward zero. In this situation, Eq. 2-14 becomes:

$$\theta_m = \begin{cases} \sum_{n=0}^{\infty} \frac{2}{\lambda_n^2} \exp(\lambda_n x^+); \quad x^+ < 0 \quad (pre-flame) \\ \sum_{n=0}^{\infty} \frac{2}{\lambda_n^2} \exp(-\lambda_n x^+); \quad x^+ \geq 0 \quad (post-flame) \end{cases} \tag{2-19}$$

Eq. 2-19 can be re-written as follows

$$\theta_m = \begin{cases} \frac{2}{\pi^2}\exp(\frac{\pi x^+}{2})\,\Phi(e^{\pi x^+},2,\frac{1}{2}); & x^+ < 0 \quad (pre-flame) \\ \frac{2}{\pi^2}\exp(-\frac{\pi x^+}{2})\,\Phi(e^{-\pi x^+},2,\frac{1}{2}); & x^+ \geq 0 \quad (post-flame) \end{cases} \tag{2-20}$$

where Φ is the *Lerch transcendent*[51] defined as follows

$$\Phi(z,s,\alpha) = \sum_{k=0}^{\infty} \frac{z^k}{(\alpha+k)^s} \tag{2-21}$$

Eq. 2-20 shows that if the *Pe* number is low enough (compared to the first eigenvalue λ_1), then the solution is independent of the *Pe* number. Figure 2-3 illustrates this graphically by showing that the solutions cluster together in the low Peclet number limit.

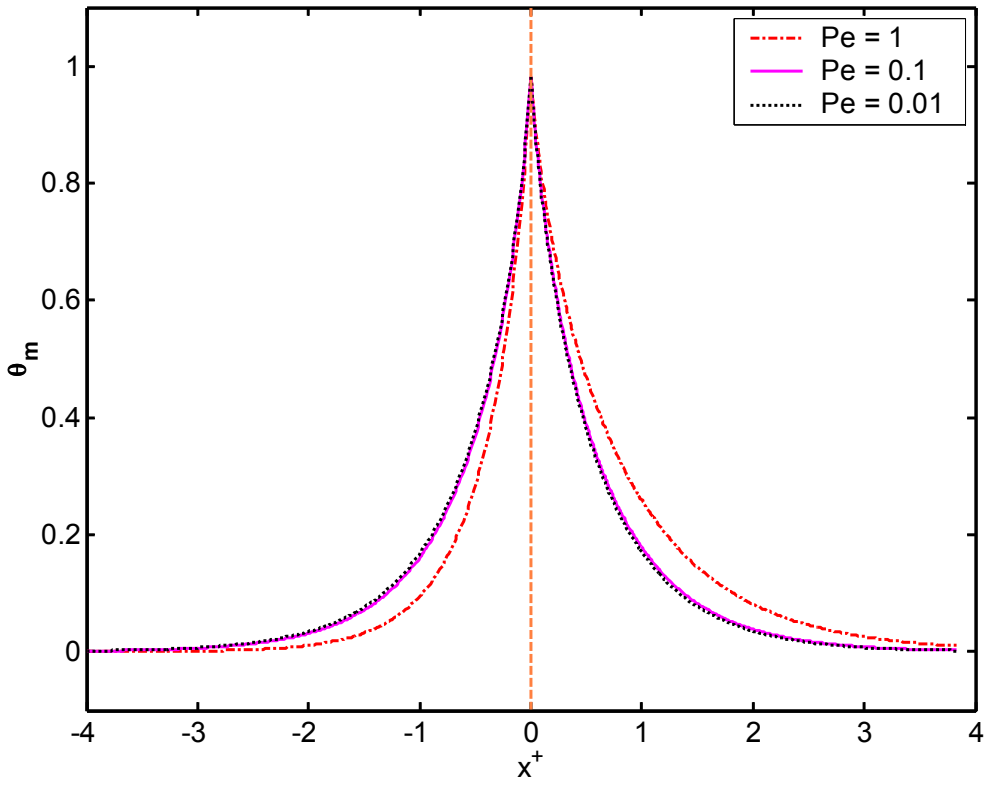

Figure 2-3: Plot of mean temperature for the low *Pe* number limit, 2D model.

What this means physically is that the convective transport term in the energy equation (which is the only term with a Peclet number) is now negligible and the problem reduces to a balance between the axial and lateral conduction terms that takes the form of a wave equation. Therefore, at small Peclet numbers, and the problem of heat transfer is entirely dominated by a balance between the heat conducted to (or from) the wall and heat conducted inside the gas.

2.6. Temperature Profiles Across the Channel:

The analytical solution obtained above enables us to determine the temperature profile across the channel at various axial locations. This is important not only for understanding the nature of the heat transfer process in the channel but for developing non-intrusive diagnostic techniques for temperature and species concentration that are based on measurements of integrated absorption along a line of sight. At this point, it is sufficient to state that if the functional form of the temperature profile along the line of sight (perpendicular to the flow direction) is known, it is possible to infer the temperature distribution along that line of sight from measurements of integrated absorbance made over a range of wavelengths. This will be explained in more detail in Chapter 4.

Most simple solutions for flows with heat transfer in a channels lead to temperature profiles with the following general functional form:

$$T(y) = A_0 + A_1 y + A_2 y^2 + \cdots + A_n y^n \tag{2-22}$$

where y is the vertical position in the channel. The solutions for simple boundary conditions like constant wall temperature and constant heat flux are often either 2nd or 4th order[52]. Therefore, the question we are interested in answering here is how well

2^{nd} and 4^{th} order polynomials in the form of eq. 2-22 represent the temperature profile across a channel in which a combustion wave is stabilized. This is important because the determination of the temperature distribution along a line of sight becomes more difficult as the order of the assumed temperature profile increases.

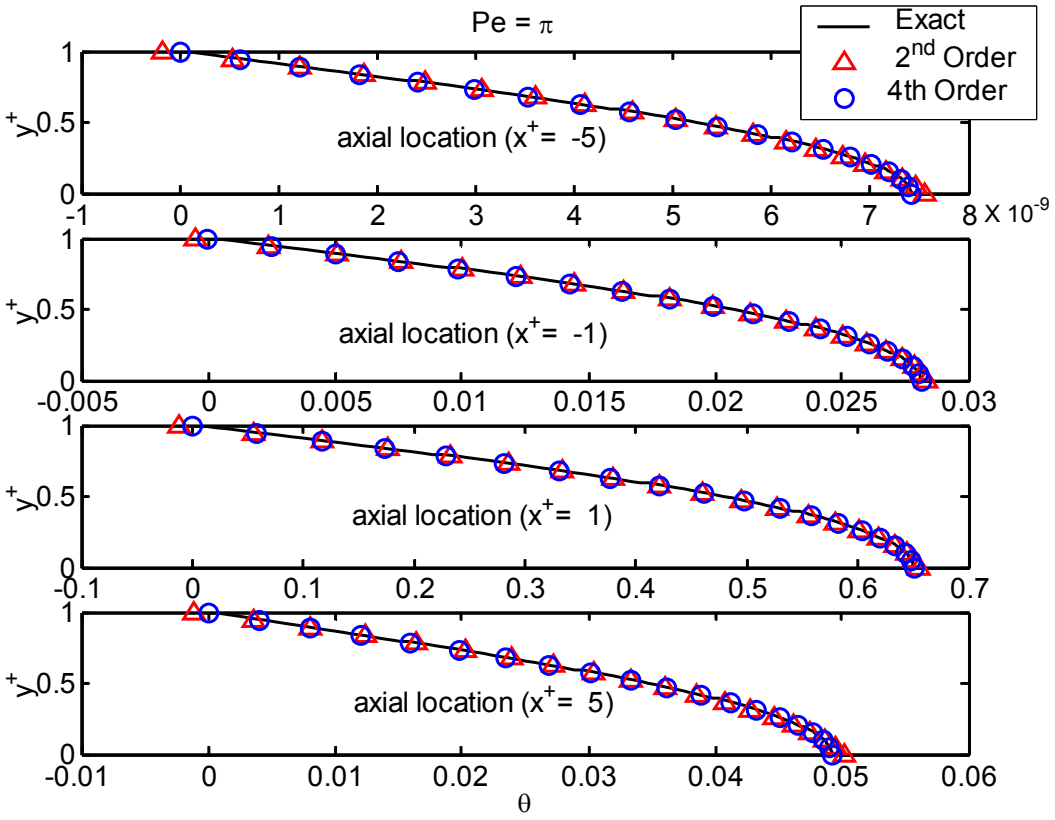

Figure 2-4: Plot of temperature profiles at different axial locations (exact and fitted polynomials); *Pe* = π

Fig. 2-4 shows temperature profiles at four axial locations for a constant *Pe* number (equal to π). The value π was chosen as it is the average of the first and second eigenvalues (usually the most significant) of the problem. The solid lines show the exact solution and the symbols show the 2^{nd} (open red triangles) and 4^{th} (open blue circles) order polynomial fits to the exact solution. The figure shows that both

polynomial fits to the analytical solution capture its behavior reasonably well. Table 2-1 provides a more quantitative comparison in terms of the value of R^2 for the fit and the slope of the temperature profile at the wall (from which heat fluxes may be computed). The table shows that the 2nd order fit matches the wall temperature reasonably well but that the 4th order fit matches the temperature and the slope reasonably well.

Axial location (x^+)	**$d\theta/dy^+|_{wall}$ (analytical model)**	**$d\theta/dy^+|_{wall}$ (2^{nd} order fit)**	**$d\theta/dy^+|_{wall}$ (4^{th} order fit)**	**R^2 (2^{nd} order fit)**	**R^2 (4^{th} order fit)**
-5	-1.16E-08	-1.4E-08	-1.2E-08	0.99923	1
-4	-5.17E-07	-6.2E-07	-5.1E-07	0.99923	1
-3	-2.29E-05	-2.7E-05	-2.3E-05	0.99923	1
-2	-0.00102	-0.00122	-0.00102	0.99927	1
-1	-0.0481	-0.0558	-0.04867	0.99973	1
1	-1.11375	-1.29127	-1.12625	0.99973	1
2	-0.547	-0.6518	-0.5446	0.99927	1
3	-0.284	-0.33928	-0.28283	0.99923	1
4	-0.148	-0.17698	-0.14751	0.99923	1
5	-0.0773	-0.09233	-0.07696	0.99923	1

Table 2-1: Comparison of fits to the analytical model; $Pe = \pi$

The effect of *Pe* number on the quality of the 2nd and 4th order polynomial approximations to the exact solution is determined by plotting temperature profiles (Fig. 2-5) and generating comparison tables (Table 2-2) for a Peclet number of unity. Again, the fitting by both polynomials is good but the 4th order does a better job with the temperature gradient at the wall.

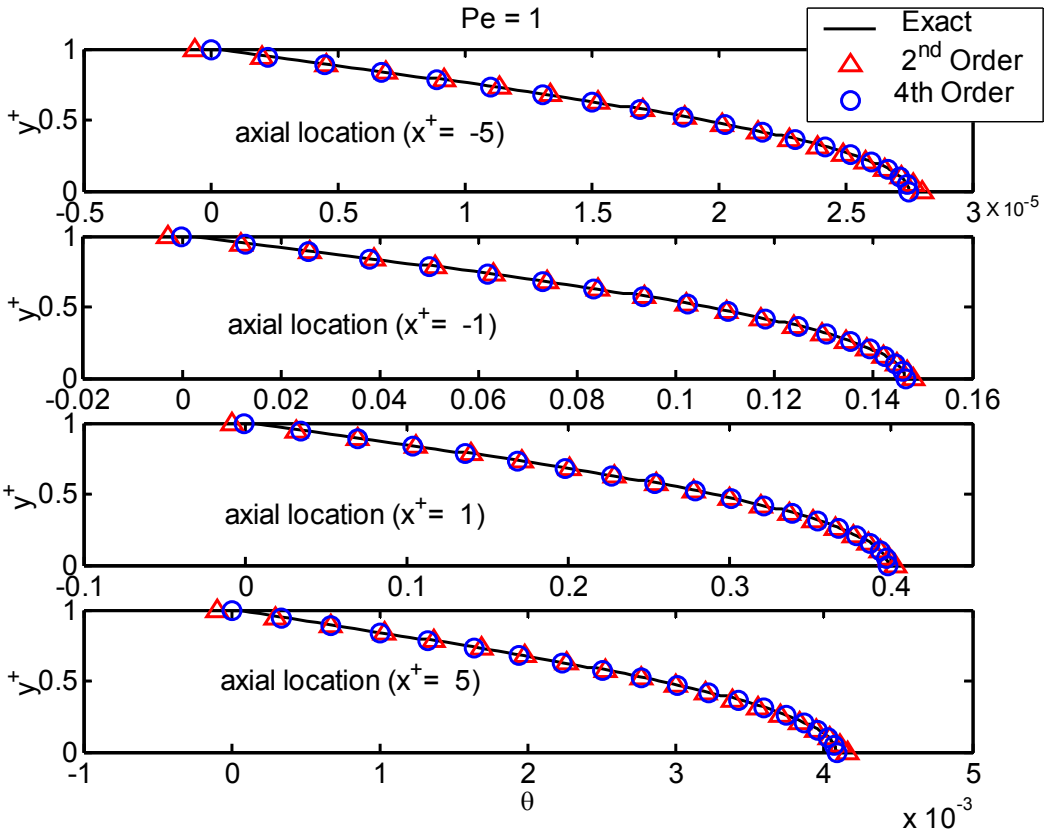

Figure 2-5: Plot of temperature profiles at different axial locations (exact and fitted polynomials); *Pe* = 1.0

Axial location (x^+)	$d\theta/dy^+\|_{wall}$ (analytical model)	$d\theta/dy^+\|_{wall}$ (2^{nd} order fit)	$d\theta/dy^+\|_{wall}$ (4^{th} order fit)	R^2(2^{nd} order fit)	R^2 (4^{th} order fit)
-5	-4.32E-05	-5.16E-05	-4.30E-05	0.99923	1
-4	-3.71E-04	-4.43E-04	-3.69E-04	0.99921	1
-3	-3.18E-03	-3.79E-03	-3.16E-03	0.99921	1
-2	-2.73E-02	-3.26E-02	-2.72E-02	0.99925	1
-1	-2.44E-01	-2.86E-01	-2.46E-01	0.9996	1
1	-6.64E-01	-7.77E-01	-6.69E-01	0.99961	1
2	-2.02E-01	-2.41E-01	-2.01E-01	0.99925	1
3	-6.38E-02	-7.62E-02	-6.35E-02	0.99923	1
4	-2.02E-02	-2.42E-02	-2.01E-02	0.99923	1
5	-6.42E-03	-7.66E-03	-6.39E-03	0.99923	1

Table 2-2: Comparison of fits to the analytical model; *Pe* = 1

2.7. Nusselt number correlation:

Finally, the exact solution for the temperature profile can be used to obtain a correlation for the variation of Nusselt number with downstream distance, which is useful for the development of numerical simulations of flows in channels, and an overall Nusselt number for the problem which is useful for simpler heat transfer calculations. The Nusselt number is defined as the ratio of the convective heat flux to the conductive heat flux. This is usually written in terms of a heat transfer coefficient h, a characteristic length scale for heat transfer L, and the thermal conductivity of the gas k:

$$Nu = \frac{hL}{k} \tag{2-23}$$

The local heat transfer coefficient is defined as

$$h_x = \frac{k\left(\frac{\partial T}{\partial y}\right)\Big|_{y=d}}{T_W - T_m} = -\frac{k}{d}\frac{\left(\frac{\partial \theta}{\partial y^+}\right)\Big|_{y^+=1}}{\theta_m} \tag{2-24}$$

Incorporating Eqs. 2-9 through 2-14 gives:

$$h_x = \frac{k}{d}\frac{\sum_{n=0}^{\infty} \exp\left(\frac{Pe \pm \sqrt{Pe^2 + 4\lambda_n^2}}{2} x^+\right)}{\sum_{n=0}^{\infty} \frac{1}{\lambda_n^2} \exp\left(\frac{Pe \pm \sqrt{Pe^2 + 4\lambda_n^2}}{2} x^+\right)} \tag{2-25}$$

Substituting Eq. 2-25 into Eq. 2-23 and taking the characteristic length scale to be the passage half height d gives:

$$Nu_x = \frac{4\,h_x\,d}{k} = 4\frac{\sum_{n=0}^{\infty} \exp\left(\frac{Pe \pm \sqrt{Pe^2 + 4\lambda_n^2}}{2} x^+\right)}{\sum_{n=0}^{\infty} \frac{1}{\lambda_n^2} \exp\left(\frac{Pe \pm \sqrt{Pe^2 + 4\lambda_n^2}}{2} x^+\right)} \tag{2-26}$$

As x^+ becomes very large, $Nu_{\pm\infty} = \pi^2$. This is the same as for the case of a thermally fully developed slug flow[31] between two infinitely long, constant temperature parallel plates. This is consistent with the fact that the model problem under consideration is indeed a slug flow with constant temperature walls and a heat source (the flame) at the origin. Therefore, we would expect the Nusselt number to asymptote to the afore mentioned case far away from the flame.

Chapter 3: Experimental Apparatus

3.1. Experimental Setup:

Fig. 3-1 is a schematic diagram of the overall experiment. Two UFC-3000A mass flow controllers (MFCs) from Unit Instruments control the flow of fuel (methane) and oxidizer (air) into a mixing chamber consisting of a 1-1/4 inch diameter steel pipe filled with steel wool.

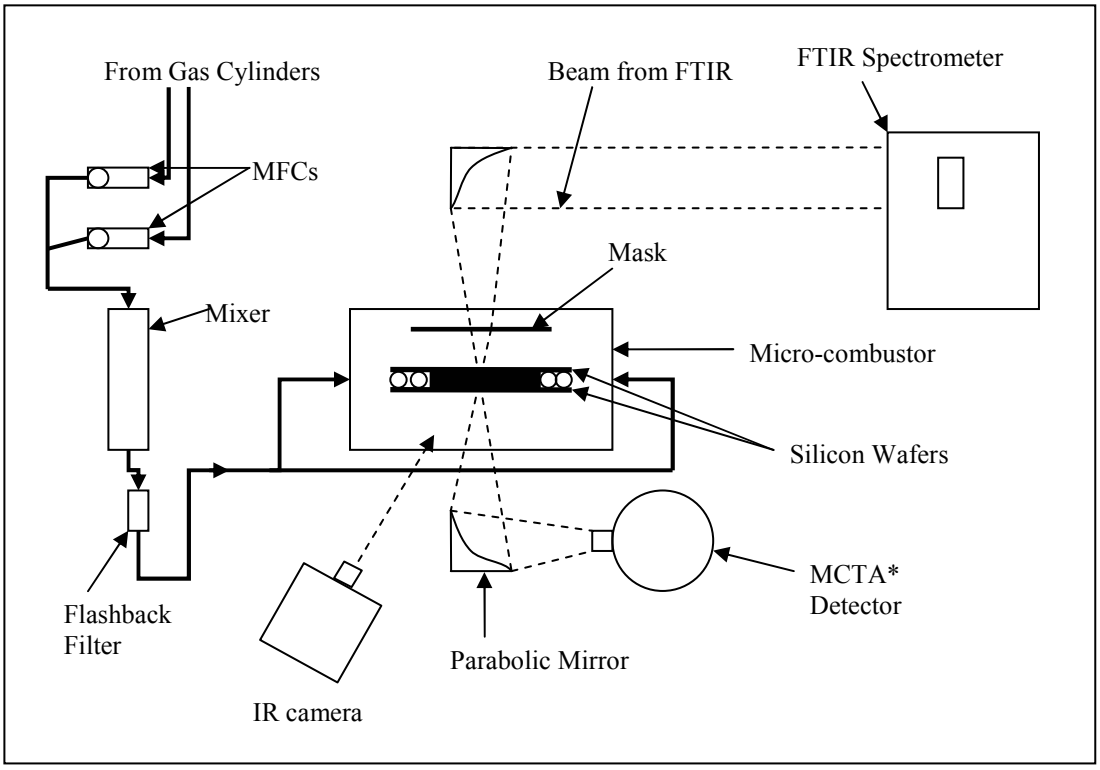

Figure 3-1: Schematic diagram of experiment.

The gas mixture exiting the chamber passes through a 15 μm Millipore filter that serves as a flash arrestor before it enters the burner plenum. The MFCs are calibrated during each run using a Drycal DC-Lite positive displacement flow meter.

3.2. Simulated Microcombustor:

The burner (Fig. 3-2) itself consists of two silicon plates attached to movable supports which allow the gap between the plates to be varied from 500 μm to 50 mm. Two vertical guides support the plates on the outside and a set of 4 vertically-oriented stainless-steel tubes (two at each wafer edge) support the wafers from the inside.

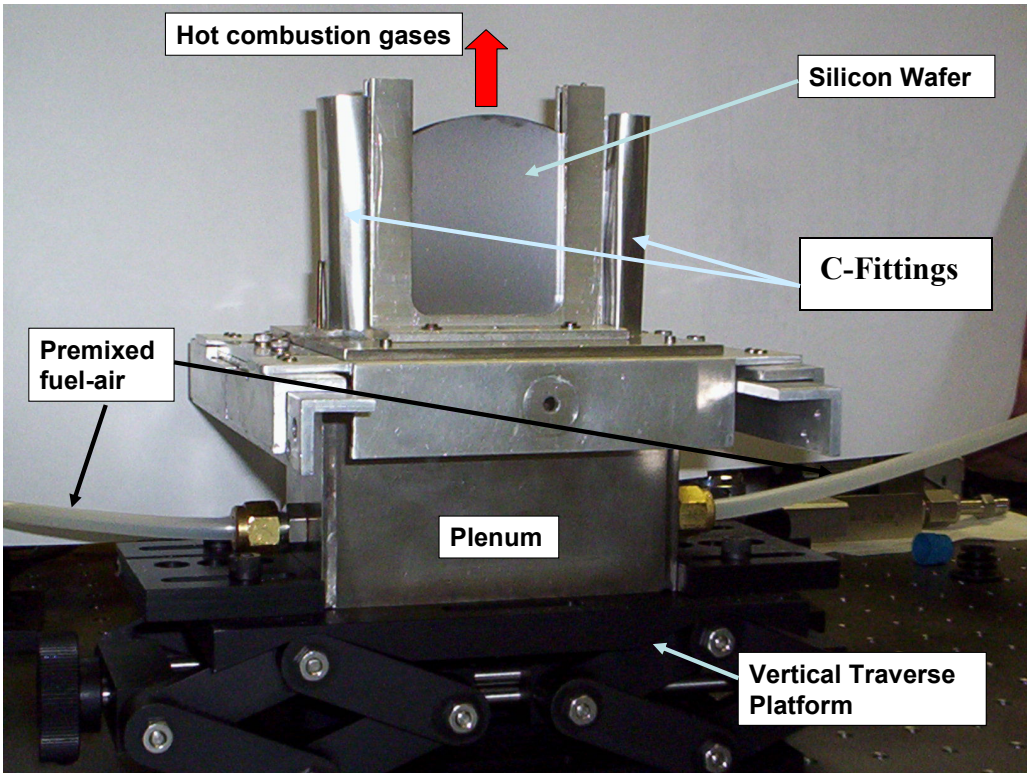

Figure 3-2: Simulated micro-combustor mounted on a vertical traverse

The diameter of the internal stainless-steel tubes (2 mm in this work) fixes the minimum wafer spacing. Compliant packings of glass wool are held in place along the outside edges of the plates by loose-fitting 'C' shaped metal retainers (see Fig. 3-2). Together, the stainless steel tubing and the glass wool insulation provide an effective barrier to leakage and/or entrainment from the edges of the plate as the flow passes vertically upward between them.

The silicon plates are constructed from ordinary silicon wafers used for MEMS micro fabrication. Two types of wafers are used in this experiment: a p-type wafer doped with boron that has both sides polished, and an n-type wafer doped with phosphorous with only a single side polished. Both wafer types are described as 'lightly' doped by the manufacturer but the specific level of doping is unknown. The wafer electrical resistivity is 10-100 Ω–cm for both types of wafers, the thickness is 500 μm, and the crystallographic orientation is 100.

3.3. External Optical System:

As illustrated previously in Fig. 3-1 the beam from a Thermo Nicolet Nexus 870 Fourier transform infrared spectrometer (FTIR) is brought to a focus inside the simulated microcombustor using a 190 mm focal length off-axis parabolic mirror.

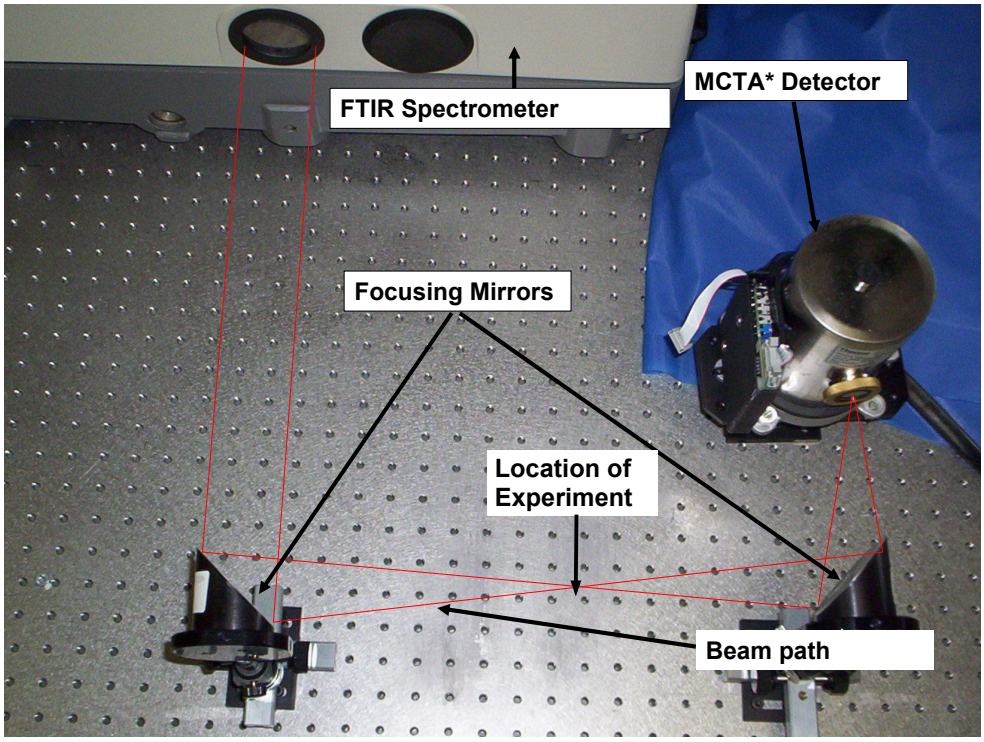

Figure 3-3: External optical arrangement (IR beam path in red)

The off-axis mirror reduces the beam diameter from approximately 38 mm to 10 mm. Fig. 3-3 is an actual photograph of the external optical system. The IR beam from the FTIR spectrometer is illustrated in red. This beam passes through the simulated microcombustor, is collected by a parabolic mirror with a focal length of 50.8 mm, and is focused onto the FTIR's Mercury Cadmium Telluride (MCTA*) detector that has been removed from the instrument cabinet and attached to the optical bench.

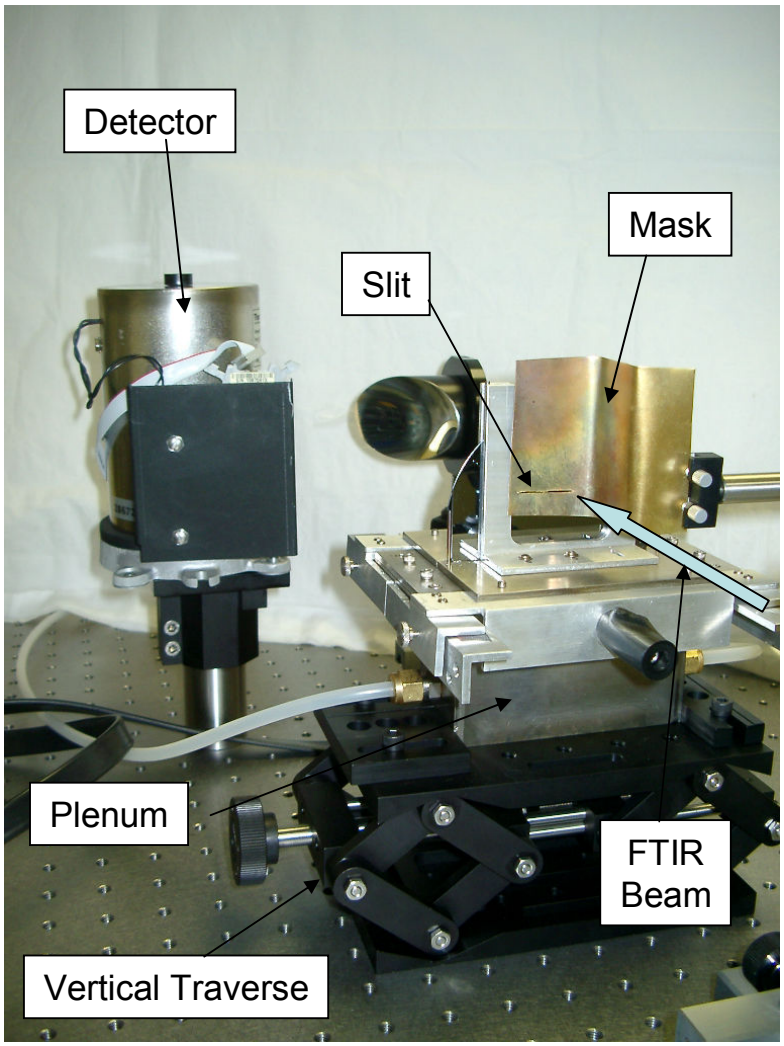

Figure 3-4: Side view of optical system.

As mentioned previously the IR beam emerging from the spectrometer gets focused down to a beam of about 10 mm diameter by the first focusing mirror. However, the streamwise spatial resolution while making these measurements would be desired to be as low as possible while preserving sufficient signal strength to observe absorption spectra different from the noise generated by the spectrometer. This is achieved by means of a spatial filter (mask with a 1mm slit), as shown in Fig. 3-4, which further reduces the size of the beam so that it extends 1 mm in the flow direction and 5 cm in the span wise direction. The microcombustor is mounted on a vertical jack that enables making measurements at different streamwise locations without adjusting the external optics.

3.4. Experimental Procedure:

The premixed methane and air mixture is supplied to the plenum below the plates. The equivalence ratio and the velocity of the flow are controlled by means of the mass flow controllers. A stainless steel screen stretched across the discharge slot of the plenum flattens the velocity profile of the flow entering the plate gap and serves as a flashback arrestor. The mixture is ignited with the silicon plates at the desired spacing (~ 2mm). The flame initially stabilizes on the outer lip of the burner. The silicon plates are heated by an external heat gun which raises the temperature of the plates and allows the flame to stabilize inside the channel. The heat gun is then stopped and the combustor is allowed to equilibrate to its final state with a flame standing inside the channel between the two silicon plates.

Once the combustor reaches equilibrium (after about 40 minutes after the heat gun is stopped) the external optical system is fine tuned to obtain maximum signal at the

detector and the FTIR spectrometer is operated to make absorption measurements. The spectra are averaged over 100 scans and are captured over a time frame of a minute. The vertical traverse is employed to allow spectra to be acquired at various points along a streamline in the pre-flame, flame, and post-flame regions.

An Omega 0.01" diameter k-type ungrounded thermocouple with a stainless steel sheath is used to measure the temperature of the silicon plates at a single point through direct contact. This is used to calibrate measurements of the surface temperature distribution across the plates made using a FLIR Systems SC3000 infrared camera.

Chapter 4: Gas-Phase Absorption Spectroscopy

4.1. Physics of Absorption:

4.1.1. Qualitative Description of Absorption:

The total internal energy of a molecule is partitioned in four types of units. The largest units of energy are stored in the nuclear partition which is related to the structure of the bond between atomic nuclei. The next largest units of energy are stored in electronic modes which are related to the configuration of the electron cloud surrounding the nuclei. This is followed by vibrational modes which are related to the vibrations of the nuclei with respect to each-other and the smallest units of energy are stored in rotational modes related to the rotation of the nuclei about each-other. Within each energy storage mode there are discrete energy levels or 'states' identified by nuclear, electronic, rotational, and vibrational quantum numbers. Changes in total internal energy correspond to transitions between these energy levels. Because the energy levels are discrete, the total internal energy can only change in discrete amounts. Therefore, when a photon (or packet of energy representing the energy present in light) strikes a molecule, it can only be absorbed by the molecule if its energy matches the difference in energy between two states and that transitions between the two states are allowed quantum-mechanically. The allowed transitions correspond to the peaks in a molecule's absorption and emission spectra.

The energy associated with the transition determines the wavelength at which it appears in the spectrum. For most molecules, nuclear transitions correspond to relatively high energy photos in the far UV or near x-ray region, electronic transitions

occur in the UV-visible range, vibrational transitions in the visible to infrared region and rotational transitions in the infrared.

Since each molecule has a unique structure, it also has a unique absorption spectrum which can be used to identify the presence of the molecule in a sample. In addition, the size and shape of the absorption spectrum are related to the molecule's concentration and temperature. Therefore, measuring the absorption spectrum of a particular molecule in a gas enables one to determine the concentration of the molecule in the sample and the gas temperature.

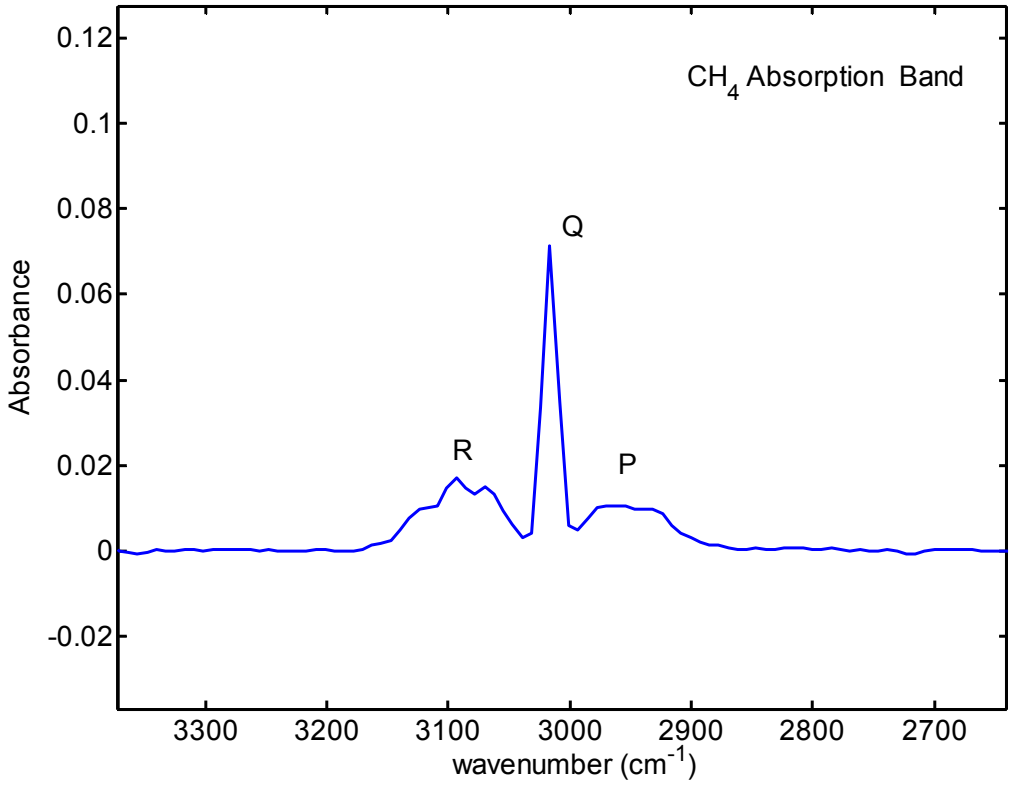

Figure 4-1: Rotational bands in CH_4 spectrum

The CH_4 rotational spectrum consists of three rotational bands namely the P, Q and R branches. Fig. 4-1 shows the absorption spectrum of CH_4 marking out each

of the rotational bands. The rotational bands correspond to transitions[53, 54] with ΔJ = -1, 0 and 1 respectively. Where J is a quantum number associated with rotational transitions.

In this work, however, we are primarily concerned with the infrared spectrum of the CO_2 molecule which arises from four vibrational modes as illustrated in figure 4-2. CO_2 is a linear molecule and has two stretching (symmetric and asymmetric) and two bending (degenerate) modes. The symmetric stretching mode is excited by photons at 2350 cm^{-1}.

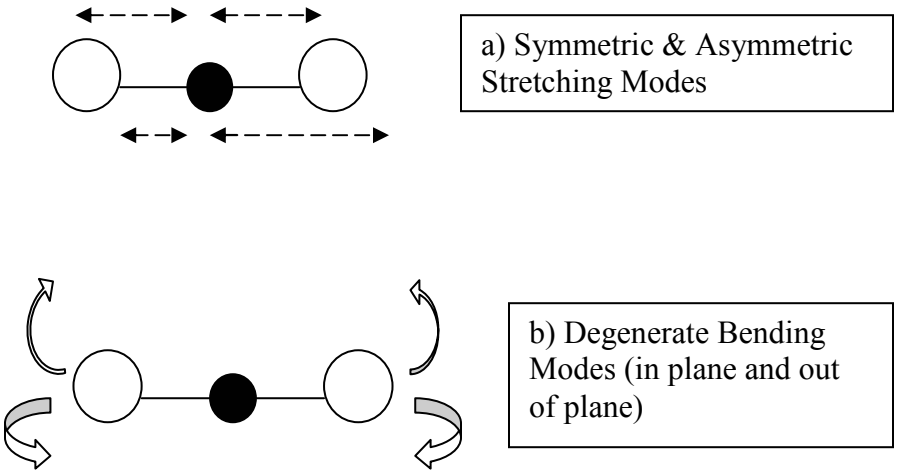

Figure 4-2: Illustration of CO_2 stretching and bending modes.

4.2. Species Concentration Measurements (CH_4 and CO_2):

The Beer-Lambert law[55] relates the change in intensity of a beam of light passing through a gas column of length dx to the concentration C of the absorbing gas molecules in moles/liter:

$$\frac{dI(\nu)}{I_0(\nu)} = -k(\nu)Cdx \tag{4-1}$$

In this equation, I_0 is the initial light intensity; dI is the measured change in transmitted intensity due to absorption by the sample along the optical path of length dx, ν is the optical frequency (typically in cm^{-1} for infrared measurements) and $k(\nu)$ is an absorption coefficient that depends on the optical frequency. Integrating over the total length of the optical path L and converting natural logarithms to base l0 leads to the definition of the molecular absorbance $A(\nu)$:

$$\log_{10}\frac{I(\nu)}{I_0(\nu)} = A(\nu) = \varepsilon(\nu)CL \tag{4-2}$$

where $\varepsilon(\nu) = -2.306k(\nu)$. The molar absorptivity $\varepsilon(\nu)$ is also a function of optical frequency. The fact that the absorbance is proportional to the path length L presents a challenge at the micro-scale, where path lengths are reduced to a few millimeters or less. This is balanced, however, by the fact that many of the species of interest (CO, CO_2, H_2O, and CH_4) are present in relatively large concentrations. Previous work has shown that it is possible make useful measurements of major species concentrations over path lengths of 1 mm or less[47].

While Eq. (4-2) could be used to infer concentration from an absorption measurement made at a single wavelength associated with a single ro-vibrational transition, more reliable results are obtained if measurements of absorption over many transitions are considered. As a result, concentration measurements are usually made by measuring the integrated absorbance $\overline{A}_{band}$, which is simply the integral of the absorbance over the entire absorption band:

$$\overline{A}_{band} = \int_{band} \varepsilon(\nu) CL d\nu = \overline{\varepsilon} CL \,. \tag{4-3}$$

In these experiments the FTIR acquires the absorption spectrum and computes the integral in Eq. (4-3), determining $\overline{A}_{band}$. The concentration in Eq. (4-3) can also be written in terms of the mole fraction X using the ideal gas law:

$$C = X \frac{P}{R_u T} \,. \tag{4-4}$$

During calibration, the product $\overline{\varepsilon} L$ in Eq. (4-3) is determined by introducing mixtures of known concentrations into the burner, measuring the resulting absorbance from 100 co-added scans, and plotting $\overline{A}_{band}$ vs. concentration.

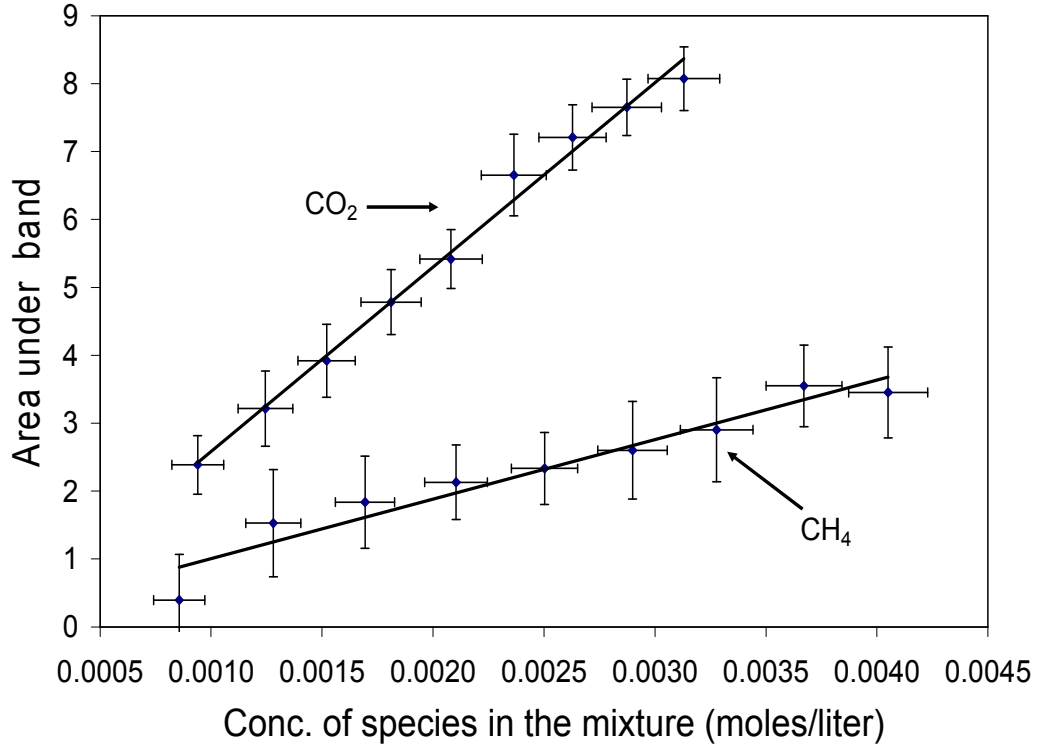

Figure 4-3: Calibration for concentration measurements (CO_2 and CH_4) at 2.15 mm wafer spacing.

Fig. 4-3 shows plots for CO_2 and CH_4 illustrating the linear dependence of absorbance on concentration expected from the Beer-Lambert's law. In situ calibration with respect to the product $\bar{\varepsilon}L$ avoids errors associated with determining the path length which could otherwise be significant at these scales. The calibration relations for the CO_2 and CH_4 concentrations as a function of integrated absorbance measured by the FTIR are:

$$C_{CO_2} = 4.02\times10^{-4}\ \overline{A}_{band} - 5.07\times10^{-5} \quad \text{(mol/l)} \tag{4-5}$$

$$C_{CH_4} = 1.37x10^{-3}\ \overline{A}_{band} - 2.27\times10^{-4} \quad \text{(mol/l)} \tag{4-6}$$

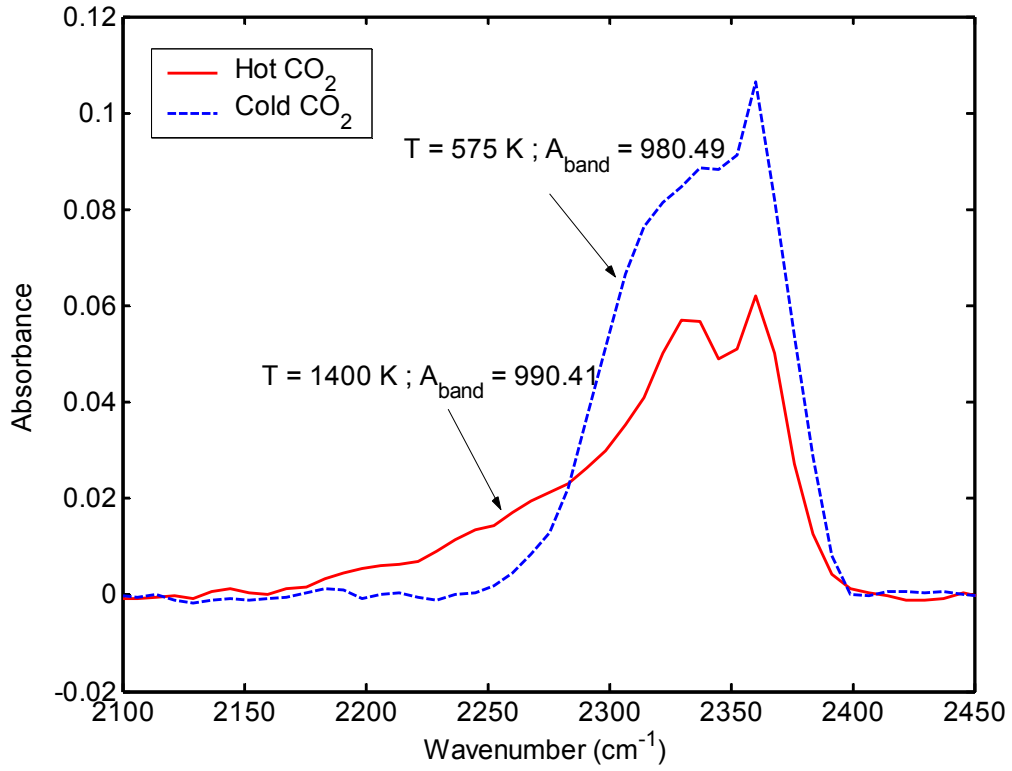

Figure 4-4: Sample hot versus cold CO_2 spectra, measured at 16 cm^{-1} resolution.

It can be noted that the x-intercepts in Eqs. (4-5) and (4-6) are zero within the estimated uncertainty of the measurements. Also, the error introduced by assuming that $\bar{\varepsilon}$ remains constant with changes in temperature is small. This is because $\bar{\varepsilon}$ is a relatively weak function of temperature and the vibrational populations of the molecules being studied are relatively weakly perturbed at combustion temperatures. This is clear from the measured spectra in Fig. 4-4 which show that increasing the gas temperature by 825K changes the integrated area under the absorption band, and hence the integrated absorbance, by only 1% (from 980.5 cm^{-1} to 990.41 cm^{-1}).

4.3. Gas Temperature Measurements:

The population of each rotational state is related to the Boltzmann population fraction of the particular transition being probed[54]. As the temperature increases, transitions associated with higher energy levels become more populated and this causes the CO_2 spectrum to broaden and flatten as illustrated in Fig. 4-4. The net result is that while the total area under the spectrum $\overline{A}_{band}$ is relatively insensitive to temperature, $A(\nu)$ changes significantly with temperature, and it is this property that is used to infer the gas temperature from the absorption spectrum.

There are two approaches to modeling the temperature dependence of the absorption spectrum. High resolution models like HITRAN[41] and HITEMP[56] provide data for the location and temperature dependence of individual spectral lines associated with particular ro-vibronic transitions. These individual lines, when added together and viewed at relatively coarse resolution ($\Delta\nu \sim 10 cm^{-1}$), form the bands shown in Fig. 4-4. In contrast, low resolution models like EM2C[44] describe the temperature dependence of the overall band shape. While high resolution models

provide much more spectral detail, they require detailed knowledge of the temperature dependence of individual spectral lines. Unfortunately, reliable data is not available for most lines at temperatures greater than about 1200K. Recent work[40] has shown that wide band models are more reliable for inferring temperature from infrared spectra in combustion flows, and so that is the approach taken here.

The wide band model is implemented using EM2C, a FORTRAN program with associated spectral databases developed by EM2C laboratories to compute the radiative intensity and transmissivity of a non-isothermal, non-homogeneous gas column consisting of mixtures of gases like H_2O, CO_2, CO etc. These calculations are accomplished by discretizing the optical path into *n* homogeneous isothermal elements using the Malkmus[56] statistical narrow band model and the Curtis-Godson approximation at a spectral resolution of 25 cm^{-1}.

The Malkmus model assumes Lorentz line shapes averaged over a wide spectral interval and that the individual column elements are homogenous and isothermal. For a given column length L (cm), total pressure p (atm), and mole fraction X of absorbing gas, the transmissivity $\bar{\tau}^{\Delta\nu}$ over the spectral interval $\Delta\nu$ (in this case 25 cm^{-1}) is given by:

$$\bar{\tau}^{\Delta\nu} = \exp\left[-2\frac{\gamma}{\delta}\left(\left(1+XpLk\frac{\delta}{\gamma}\right)^{1/2}-1\right)\right] \tag{4-7}$$

In this expression, k (cm^{-1} atm^{-1}), δ (cm^{-1}) and γ (cm^{-1}) are the model parameters for the particular molecular species under consideration. The Curtis-Godson approximation involves replacing k and γ/δ in Eq. (4-7) with average values of these parameters over the particular spectral interval being considered. The input

parameters for the EM2C model come from the HITRAN database and supplementary data for k, $1/\delta$, and γ obtained by EM2C laboratories. In the work reported here, we focus on absorption by CO_2 since it is naturally produced in the flame and gives a relatively strong signal.

Gas temperature measurements are made by fitting $A(\nu)$ for CO_2 predicted by the EM2C code to $A(\nu)$ observed in the experiments. This is accomplished in MATLAB using a Newton-Gauss algorithm and a least squares fitting routine 'lsqcurvefit'. The Newton-Gauss algorithm calls the EM2C FORTRAN program with initial guesses for the gas temperature and CO_2 concentration. The residual is computed based on the difference between the experimental spectrum and the model prediction. The routine perturbs the values slightly to find the largest gradient for the input parameters of temperature and concentration, and uses the direction of the gradient to iterate forward to find the values of concentration and temperature that best fit the experimental spectrum. The temperature corresponding to the best fit is taken to be the gas temperature. The resolution of the measurements is 16 cm^{-1} while the resolution of the EM2C model is only 25 cm^{-1}. As a result, the output of the EM2C model must be interpolated onto the experimental data before the residual is computed.

4.4. Principle of Operation of FTIR Spectrometer:

A Fourier transform infrared (FT-IR) spectrometer consists of a broadband infrared source (usually a heated filament), a Michelson interferometer, a sample compartment, and a detector as illustrated in Fig. 4-5.

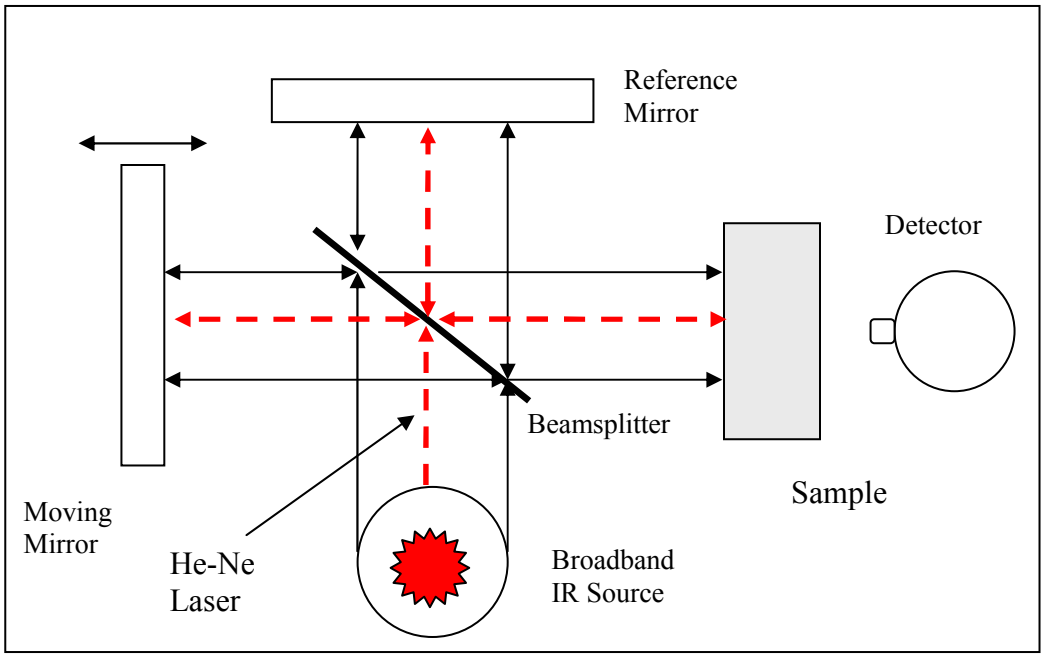

Figure 4-5: Sketch of FTIR showing its main components (Michelson interferometer)

The Michelson interferometer is a tunable optical filter that is transmissive in only narrow spectral regions as illustrated in Fig. 4-6. Each peak in the transmission spectrum corresponds to an 'order' of the interferometer and the width of each peak in the transmission spectrum corresponds to the interferometer's spectral resolution. Moving the mirror shifts the output spectrum to the left or right in the figure. A complete scan of all wavelengths is accomplished by moving the mirror sufficient distance so that the peaks in the absorption spectrum overlap their starting positions.

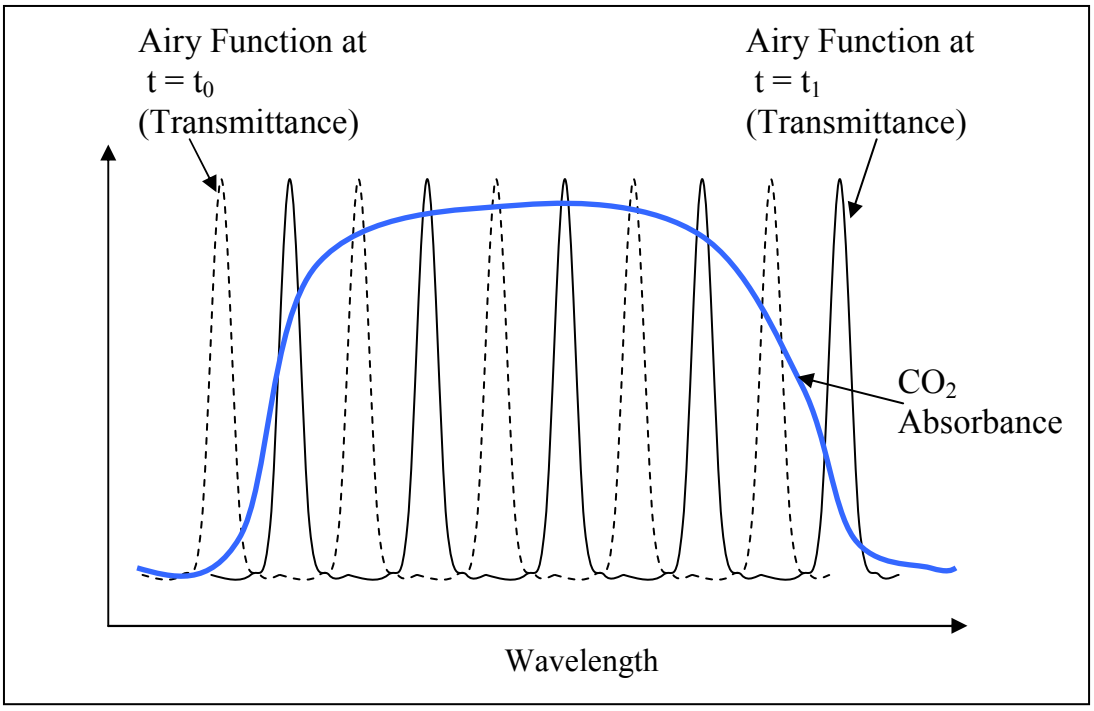

Figure 4-6: Functioning of a Michelson interferometer.

The basic idea of a Fourier Transform Infrared Spectrometer (FTIR) is to move the mirror with certain speed thereby sweeping a light beam with a very narrow spectral line width (typically 0.02 cm^{-1}) over the absorption features of the sample. Recording the signal from the detector (which corresponds to transmitted intensity) as a function of time and performing a Fourier transform gives the transmitted intensity as a function of optical frequency. This, in turn, can be converted to wavelength or wave number as required and used to create an absorption spectrum. The scan is controlled and calibrated by counting the passage of interference fringes in a Helium-neon laser beam that also follows the optical path through the interferometer.

Chapter 5: Uncertainty Analysis

5.1. Gas Temperature Uncertainty:

Determining the uncertainty in the fitted temperature begins by considering the residual R^2 from the temperature fitting procedure. It is computed in the following way:

$$R^2 = \sum_{i=1}^{N} \left(A_{ex,j} - A_{fit,j} \right)^2 , \tag{5-1}$$

where $A_{ex,i}$ is the ith point of the experimentally measured absorbance spectrum, $A_{fit,i}$ is the ith point of the best fit to the absorbance spectrum, and N is the total number of points defining the spectrum. The basic premise of the FTIR uncertainty analysis is to express the absorbance observed by the instrument as the sum of the 'real' absorbance (ie. the absorbance that one would measure in the absence of instrument error) and the error introduced by the instrument:

$$A_{ex,i} = A_{real,i} \pm \sigma_{rms} . \tag{5-2}$$

In these expressions, $A_{real,i}$ is the absorbance at point i in the absence of instrument errors and σ_{rms} represents the instrument errors. A similar approach is taken with the absorbance spectrum fitting procedure:

$$A_{fit,i} = A_{perfect\ fit,i} \pm \left[\left. \frac{\partial f_i}{\partial T} \right|_C \delta T + \left. \frac{\partial f_i}{\partial X} \right|_T \delta X \right]. \tag{5-3}$$

In this expression, $A_{perfect\ fit,i}$ is the absorbance at point i in the absence of fitting, measurement, *and* instrument errors while the second term represents the errors that arise from uncertainties on the inputs to the fitting procedure. In this latter term, f is

the EM2C function used to compute the absorbance as a function of gas temperature and concentration and δX is the uncertainty in the gas mole fraction which is known from the results of the previous section. δT is the desired uncertainty in the temperature measurement. Substituting Eqs. (5-2) and (5-3) into (5-1), and incorporating the fact that $A_{real,\ i} = A_{perfect\ fii,\ i}$ gives the following expression for the residual of the fit:

$$R^2 = \sum_{i=1}^{N} \left\{ \pm \sigma_{rms} \mp \left[\left. \frac{\partial f_i}{\partial T} \right|_C \delta T + \left. \frac{\partial f_i}{\partial T} \right|_X \delta X \right] \right\}^2 . \tag{5-4}$$

This expression shows that even when the fit to the experimental data is perfect ($R^2=0$) and instrument errors are zero, the uncertainty in the temperature still depends on the uncertainty in the concentration measurement.

Eq. (5-4) can be re-written as

$$R^2 = \left(\pm \alpha \mp \beta \delta T \right)^2 , \tag{5-5}$$

where α and β are constants that can be computed using δ_{rms}, f, and δX:

$$\alpha = \sum_{i=1}^{N} \left(\sigma_{rms} - \left. \frac{\partial f_i}{\partial X} \right|_T \delta X \right), \text{ and} \tag{5-6}$$

$$\beta = \sum_{i=1}^{N} \left. \frac{\partial f_i}{\partial T} \right|_X . \tag{5-7}$$

Expanding Eq. (5-5) gives the following quadratic relationship between R^2 and δT:

$$R^2 = \alpha^2 - 2\beta\delta T + \beta^2 \left(\delta T \right)^2 \tag{5-8}$$

Before solving Eq. (5-8) for δT, it is worth noting that it appears to have the proper behavior. When the fit to the experimental data is perfect ($R^2=0$), the uncertainty in the temperature will depend on the uncertainty in the instrument and

the concentration measurement. When the uncertainty in the instrument is zero and the data fit is perfect, the uncertainty in the temperature depends only on the uncertainty in the concentration measurement. Only when the instrument, concentration measurement, and fit are all perfect, can the uncertainty in the temperature measurement become zero.

Solving Eq. (5-8) for δT using the quadratic formula gives:

$$\delta T = \frac{1 \pm \left(1 - \left(\alpha^2 - R^2\right)\right)^{1/2}}{\beta} \tag{5-9}$$

There are two solutions to Eq. (5-8) and the larger is taken as the uncertainty in the temperature. The asymptotic behavior of Eq. (5-9) shows that as $\alpha, R \to 0$, $\delta T \to \left(0, 2/\beta\right)$. Since we choose the larger of the two solutions, the error does not necessarily go to zero as $\alpha, R \to 0$. In order to drive the uncertainty in temperature to zero in all cases, we need $\beta \to \infty$. In other words, we need to choose a spectral region with infinite temperature sensitivity. Conversely, Eqs. (5-7) and (5-9) show that when the temperature sensitivity of the spectral region goes to zero, the uncertainty in temperature goes to infinity.

Chapter 6: Challenges in Implementing Technique

6.1. Interference from Silicon:

Fig. 6-1 compares the absorption spectra of CO_2 and CH_4, with the transmission spectrum of silicon. It shows that the silicon wafer's transmissivity is approximately 60% except for a small region around the CO_2 band where it varies from 55% to 60%.

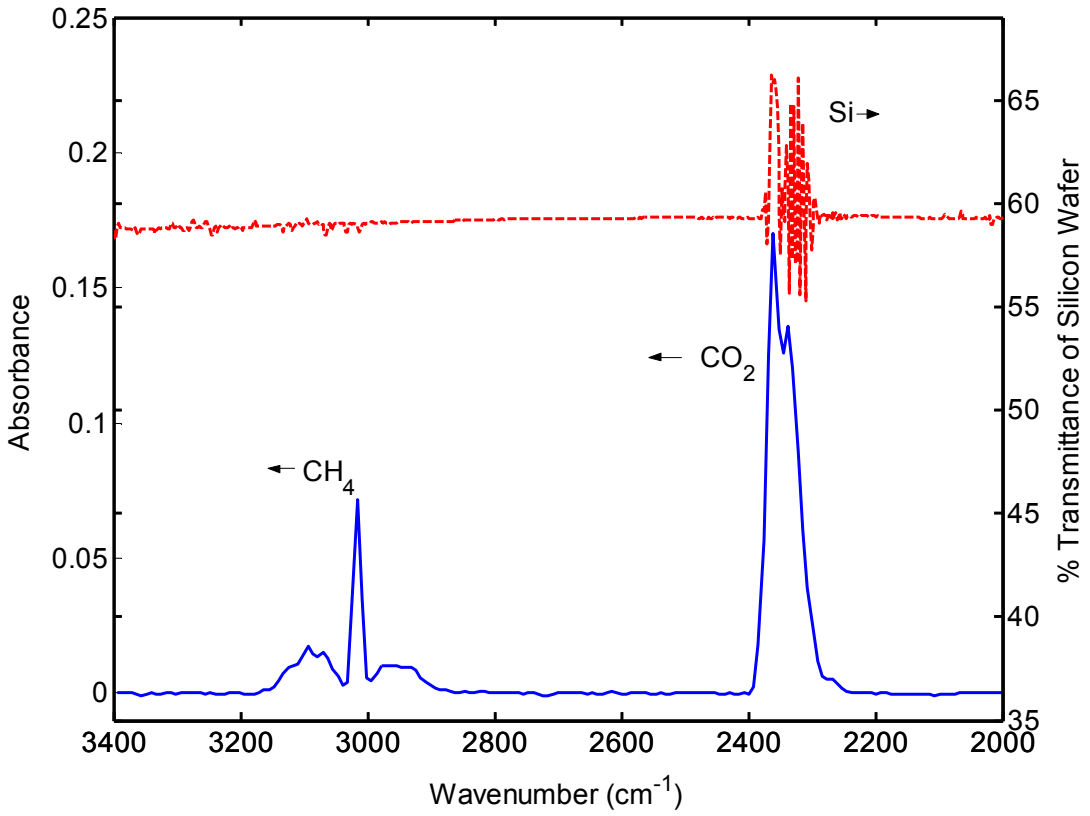

Figure 6-1: Comparison of CO_2, CH_4 (absorption) and Si (% transmittance) spectra.

This interference prevents capture of the strongest part of the CO_2 band in the 2300-2400 cm^{-1} range. The complete nature of this interference is unclear but the

'dip' in the absorption spectrum near the peak appears to be related to spectral features of both silicon and CO_2. Silicon has an atomic absorption line[57] at ~2340 cm^{-1} but experimental measurements[58] of CO_2 absorbance that are not made with silicon in the optical path (see figures 4-4, 4-8 and 4-9 of ref. [58]) also show a 'dip' in this area - one that is not predicted by EM2C. Regardless, the interference is a function of temperature that is not easily subtracted out and it causes problems when trying to fit the CO_2 band. The solution implemented here is to fit only the region of the band (2150 – 2300 cm^{-1}) that is not affected by the interference. This is illustrated in Fig. 6-2.

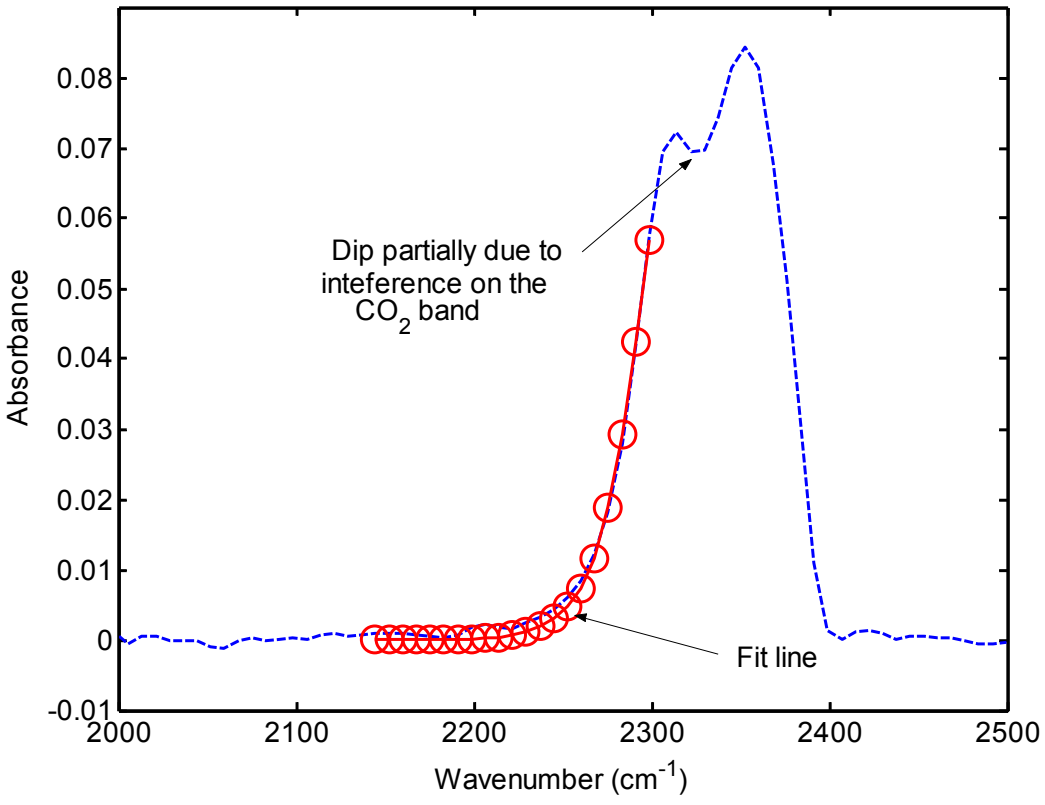

Figure 6-2: Fit of CO_2 spectra: ϕ = 0.86, U = 44 cm/s, 2.15 mm wafer spacing, 20 mm downstream from inlet.

6.2. Interference from Silicon:

Apart from the interference in the CO_2 band by silicon, additional complications arise because the IR transmissivity of silicon is also a relatively strong function of temperature[60] which necessitates making measurements of the temperature dependence of the transmissivity of the silicon plates. This was accomplished by heating the plates with a heat gun, recording the plate temperature with a sheathed k type thermocouple, and recording the absorbance measured by the FTIR.

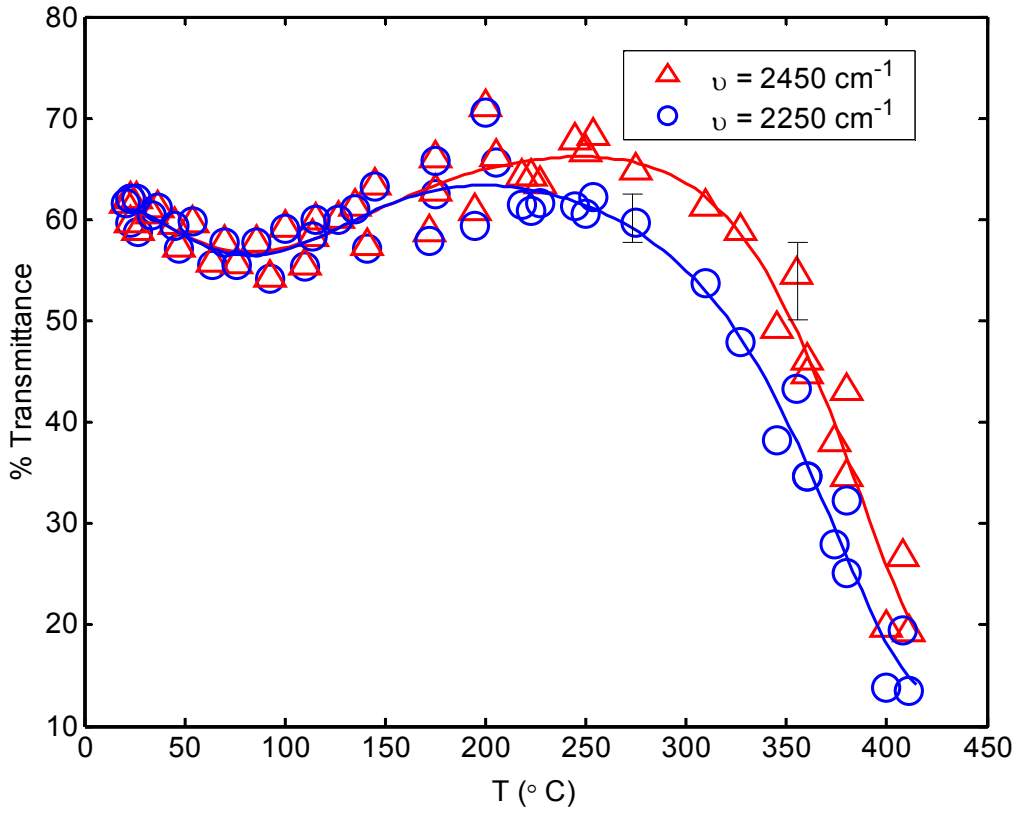

Figure 6 -3: Percent transmittance of double side polished Si wafer vs. temperature at different wave numbers around the CO_2 regime (2250 – 2450 cm^{-1}).

Since the Biot number for the silicon plates exchanging heat with the environment is < 0.01, it is reasonable to assume that the plate temperature in the region interrogated by the beam is uniform. This also enabled us to locate the thermocouple against the plate immediately outside the interrogation region so as not to obstruct the optical path.

The measured transmittance as a function of temperature at 2250 cm^{-1} and 2450 cm^{-1} is shown in Fig. 6-3. Transmittance in the spectral region around the CH_4 band varied in a similar manner. The significant scatter in this data arises primarily from inconsistencies in the thermal contact between the thermocouple and the silicon plates as the thermocouple was repeatedly pressed against the plate surface. The line drawn through the data points in this figure is a best fit polynomial. The data show that the transmittance of the silicon wafers drops dramatically with increasing plate temperature. Alone, this does not pose a problem for the diagnostic technique because a baseline shift and scaling is performed on every spectrum before it is co-added. However, the decrease in transmitted signal decreases the signal/noise ratio of the transmitted intensity measurement and therefore increases the uncertainty in concentration and temperature measurements. As a result, uncertainties in concentration and temperature increase with operating temperature because of the increasing opacity of silicon. This increase in opacity may be attributed to the increased ease with which incident IR photons may excite electrons into the conduction band as the temperature of the silicon substrate is raised. In the results presented in Chapter 7 of this paper, the peak temperature that the silicon plate

reaches is approximately 260 ^{o}C (~ 530 K). This is well below the temperature at which silicon's transmissivity begins to drop dramatically (~350 ^{o}C).

6.3. Etaloning:

When two polished silicon wafers are used to form the combustion cavity, the interference fringes illustrated in Fig. 6-4 are produced.

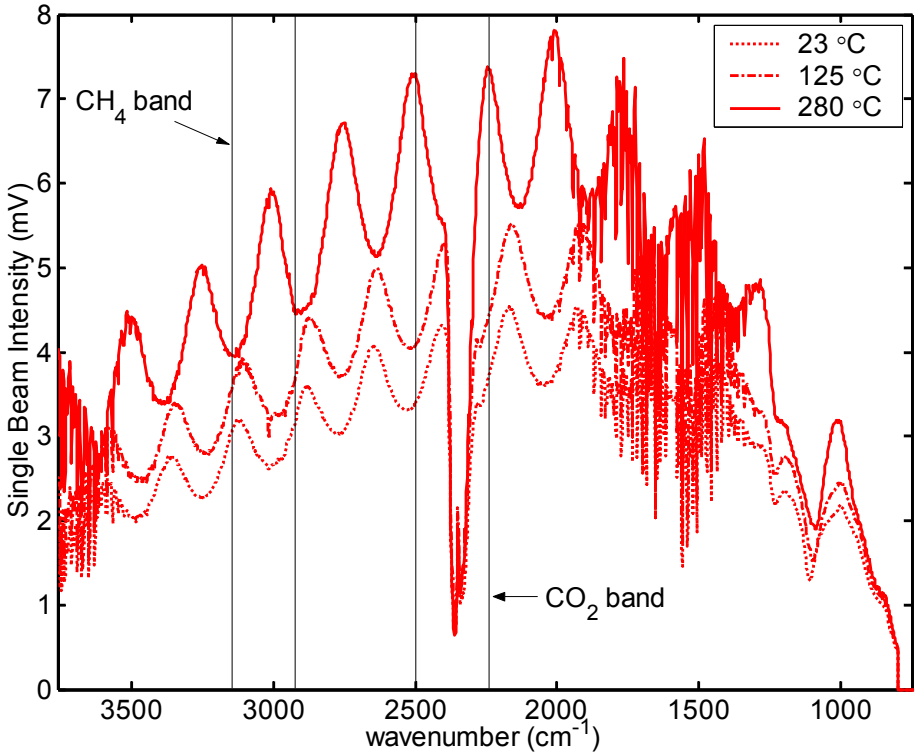

Figure 6-4: Transmission spectra of a pair of double side polished silicon plates at several plate temperatures, showing the effect of plate temperature on the interference.

The period of these fringes is on the same order as the width of the CO_2 band, and the position of the fringes shifts with changes in temperature. This interference phenomenon is disrupted in the experiments by replacing one of the double side

polished plates with a single side polished plate. The unpolished side acts as a diffuser and disrupts the 'organized' interference responsible for creating the fringes. Unfortunately, this results in a dramatic reduction in signal intensity at the detector: the single side polished plate transmits 5% whereas the plate with both sides polished transmits 60%. The single side polished plate is placed on the 'downstream' side of the path to ensure that the beam is only scattered after passing through the interrogation volume. This preserves the intended spatial resolution of the measurement.

Chapter 7: Results

7.1. Gas Temperature Measurements:

As outlined earlier, the gas temperature measurements made in this work rely on using the EM2C wide band model program to fit the experimentally measured absorbance spectrum of CO_2 to that predicted by the wide band model and obtain the gas temperature as that value for which the fit is within the prescribed tolerance. However, the EM2C program is equipped to handle a prescribed profile for the temperature along the line of slight (i.e. between the two silicon plates). The greatest advantage of doing this would be that if the order of the polynomial describing the temperature profile is known, one can couple the EM2C program with a least-squares optimizer to determine the values of the polynomial coefficients of the temperature profile that minimize the difference between predicted and measured integrated absorbance. Once the coefficients have been determined, the derivative of the temperature at the wall can be used to compute the local heat flux to the wall.

In Chapter 2 we saw that for the simplified heat transfer model used to represent the combustor investigated in this work, the exact temperature profile was well represented using 2^{nd} and 4^{th} order polynomials. In this section, we investigate the effect that the assumed functional form of the temperature profile has on the gas temperature measurements.

7.1.1. Polynomial fitting (derivations/results):

a) Zeroth order profile (uniform temperature):

Eq. 7-1 is the simplest possible functional form for the temperature distribution across the channel – a uniform profile.

$$T(y) = c_1 \tag{7-1}$$

This is equivalent to assuming the temperature distribution between the two plates is one dimensional and that it only varies in the streamwise direction.

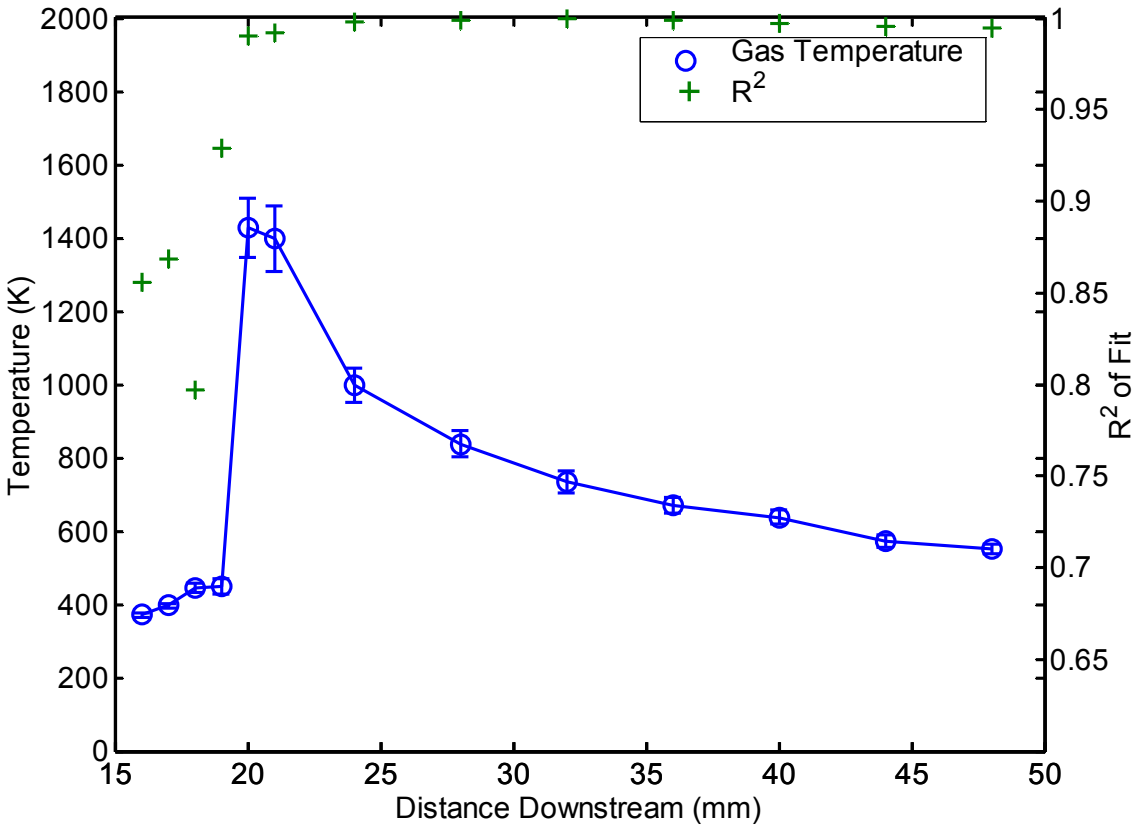

Figure 7-1: Axial gas temperature profile (open circles) and R^2 (crosses) for constant Temperature fitting. The equivalence ratio is 0.86 and the flow velocity is 44 cm/s.

Fig. 7-1 shows the plot of gas temperature as a function of streamwise distance when constant temperature profile is assumed. Also shown in the figure are the values of R^2 for the quality of the fit between the experimentally measured absorbance and the absorbance from the wide band model. The temperature profile indicates that the flame is stabilized at a downstream distance of 20 mm. However, the peak temperature is only about 1400 K which is much lower than the adiabatic flame temperature of 2093 K for this equivalence ratio. Since assuming a uniform temperature profile does not lead to reasonable results, it appears that assuming that the temperature profile is uniform is not a good approximation. Nevertheless, the temperature distribution along the length of the channel appears to be qualitatively reasonable in that the temperature increases as it approaches the flame, peaks at the flame, and decays in an exponential-like way downstream of the flame.

b) 2nd Order Profile:

Equation 7-2 gives the functional form for a second order temperature profile.

$$T(y) = a_2 y^2 + b_2 y + c_2 \tag{7-2}$$

In this expression, *y* varies from zero to *2*d*, the channel width, which in the current experiment is 2.15mm. The temperature profile is forced to be symmetric about the channel centerline by enforcing the following conditions:

$$T(0) = T(2d) \tag{7-3}$$

$$\left.\frac{dT}{dy}\right|_{y=d} = 0 \tag{7-4}$$

$$\left.\frac{dT}{dy}\right|_{y=0} = -\left.\frac{dT}{dy}\right|_{y=2d} \tag{7-5}$$

Assuming that the temperature profile is symmetric appears to be reasonable for this problem. For the 2nd order case this means that

$$b_2 = -(2d)\, a_2 \qquad (7\text{-}6)$$

Therefore, the constant b_2 of the fit is related to a_2 leaving only two free parameters namely a_2 and c_2 to iterate on to find the best fit temperature profile. Note that for polynomials higher than 4th order additional constraints on top of the three symmetry based ones would need to be supplied.

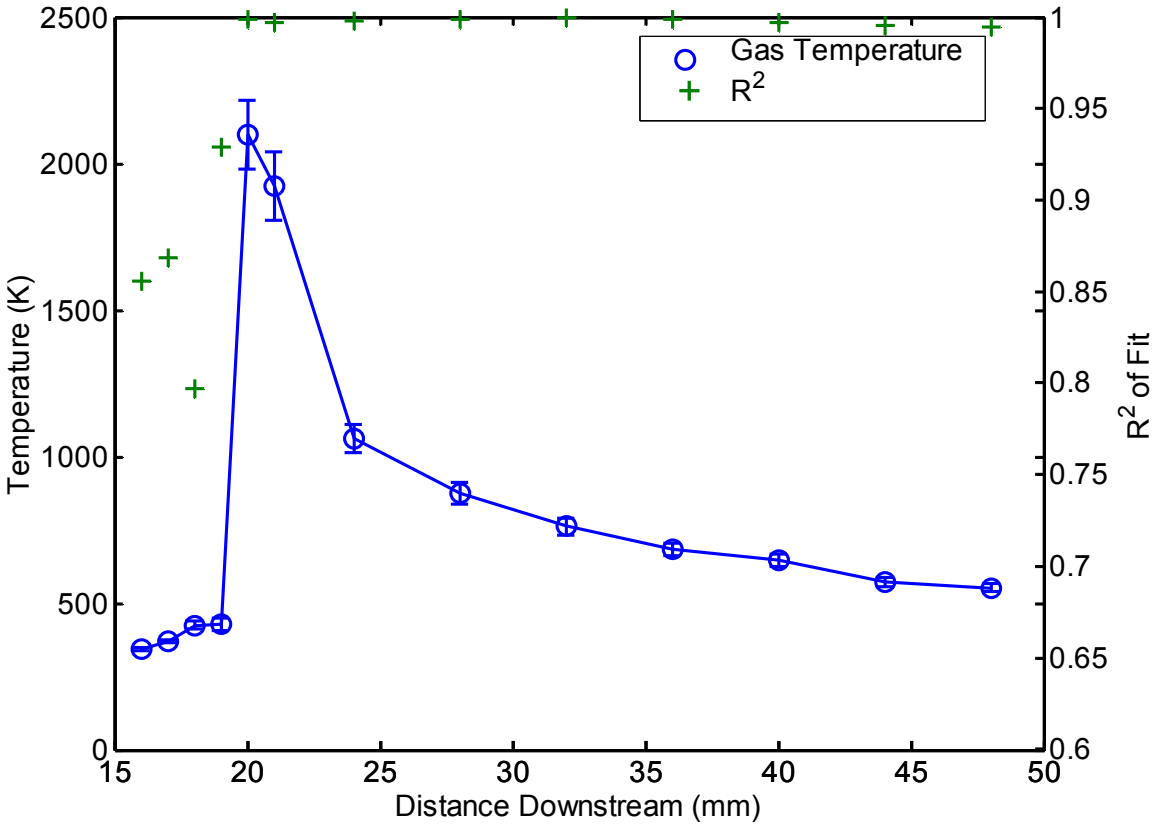

Figure 7-2: Axial peak gas temperature profile (open circles) and R^2 (crosses) for 2nd order temperature fitting. The equivalence ratio is 0.86 and the flow velocity is 44 cm/s.

As discussed in Chapter 4, the curve fitting subroutine (lsqcurvefit) is used to find the values of a_2 and c_2 that minimize the difference between the integrated absorption predicted by EM2C using the temperature profile specified by Eq. 7-2 and the integrated absorbance measured in the experiment. Once the coefficients are evaluated, the temperature profile is known. It may also be of interest to also note that when the temperature profile is second order, Eq. 7-4 is satisfied automatically once equations 7-3 and 7-5 are satisfied.

Fig. 7-2 shows the variation in peak (centerline) temperature across the channel as a function of downstream distance when a 2nd order temperature profile is assumed. The experimental data used to compute the temperature profile is the same as that used to generate Fig. 7-1. The position of the flame in Fig. 7-2 is the same as in Fig. 7-1 - 20mm downstream of the inlet – but the flame temperature is much about 2100K which is much higher than the peak flame temperature in Fig. 7-1 and quite close to the adiabatic flame temperature.

z (mm)	a_2 (K/cm^2)	b_2 (K/cm^2)	c_2 (K)
16	8.0124e+003	-1.6426e+003	425.617
17	6.8129e+003	-1.3966e+003	442.045
18	5.1543e+003	-1.0566e+003	478.303
19	5.1450e+003	-1.0547e+003	483.004
20	-1.4665e+005	3.0063e+004	556.794
21	-1.2052e+005	2.4707e+004	656.209
24	-1.6490e+004	3.3804e+003	886.885
28	-9.7132e+003	1.9912e+003	772.085
32	-7.1427e+003	1.4642e+003	686.353
36	-3.6363e+003	7.4545e+002	645.078
40	-2.4948e+003	5.1143e+002	620.563
44	-2.0481e+002	4.1986e+001	571.064
48	4.9583e+002	-1.0164e+002	555.819

Table 7-1: Sample temperature profile parameters (2nd order)

This suggests that the profile in 7-2 is more realistic than the profile in 7-1. The calculated temperature profile parameters for this example are presented in Table 7-1.

c) 4th order fitting:

Equation 7-6 gives the functional form for a second order temperature profile.

$$T(y) = a_4 y^4 + b_4 y^3 + c_4 y^2 + d_4 y + e_4 \qquad (5\text{-}6)$$

Again we use the conditions arising out of the symmetry of the burner's geometry to relate the coefficients by applying Eqs. 7-3 through 7-5.

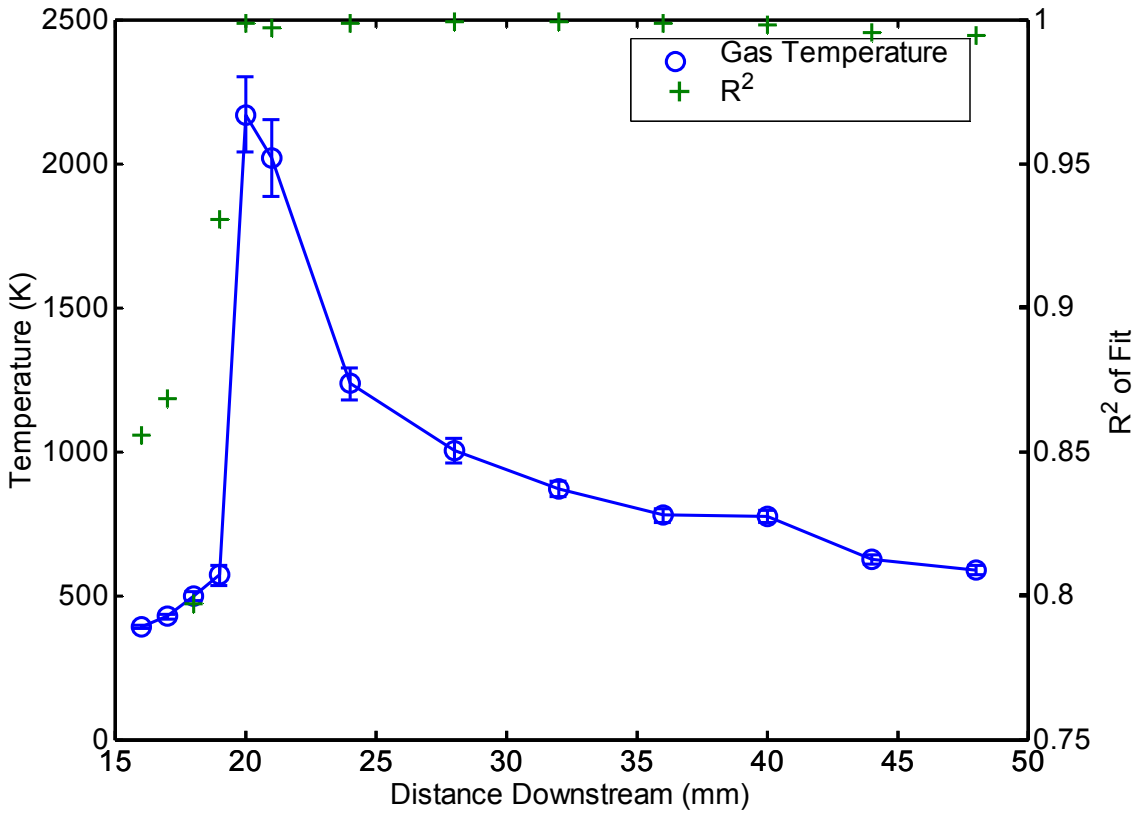

Figure 7-3: Axial peak gas temperature profile (open circles) and R^2 (crosses) for 4th order temperature fitting. The equivalence ratio is 0.86 and the flow velocity is 44 cm/s.

For the 4th order case this reduces to

$$b_4 = \frac{-(2d\,c_4 + d_4)}{2d^2} \quad and \quad a_4 = \frac{(2d\,c_4 + d_4)}{(2d)^3} \tag{7-7}$$

where c_4, d_4 and e_4 are the free parameters. Again, the curve fitting program (lsqcurvefit) is used to find the values of the free parameters that minimize the difference between the predicted and measured integrated absorbance. Fig. 7-3 is a plot of the resulting axial temperature profile along the center of the channel. The values of the peak temperatures in Figs. 7-3 and 7-2 are very similar indicating that the profiles are self-consistent. The values of the fitted parameters are presented in Table 7-2.

z (mm)	a_4 (K/cm^4)	b_4 (K/cm^3)	c_4 (K/cm^2)	d_4 (K/cm)	e_4 (K)
16	2.3246e+005	-9.9958e+004	9.5375e+003	2.5972e+002	3.4605e+002
17	2.8315e+005	-1.2175e+005	9.8109e+003	7.0470e+002	3.5161e+002
18	3.8548e+005	-1.6576e+005	1.0378e+004	1.5998e+003	3.6087e+002
19	6.7889e+005	-2.9192e+005	1.5397e+004	3.4367e+003	2.9520e+002
20	2.7320e+006	-1.1747e+006	2.3674e+004	2.2061e+004	6.1945e+002
21	2.2739e+006	-9.7778e+005	1.4762e+004	1.9425e+004	6.6915e+002
24	1.0750e+006	-4.6223e+005	1.1996e+004	8.1041e+003	6.5600e+002
28	8.2889e+005	-3.5642e+005	1.0560e+004	5.9676e+003	5.7222e+002
32	7.8705e+005	-3.3843e+005	1.2096e+004	5.2213e+003	4.8424e+002
36	5.2963e+005	-2.2774e+005	4.9071e+003	4.2086e+003	4.7991e+002
40	8.2231e+005	-3.5359e+005	1.4598e+004	5.0339e+003	3.9286e+002
44	3.5342e+005	-1.5197e+005	8.8127e+003	1.6177e+003	4.9112e+002
48	2.7395e+005	-1.1780e+005	8.1955e+003	9.6060e+002	5.0008e+002

Table 7-2: Sample temperature profile parameters (4th order)

7.1.2. Convergence Testing:

The optimization procedure that adjusts the free parameters in the temperature profile to best fit the experimental measurements requires an initial guess for the

values of the free parameters. For the solutions to be reliable, the final values of the free parameters should be independent of the initial guesses within 'reasonable' limits. In this section we investigate the effect of the initial guesses on the temperature profile.

a) Constant Temperature:

Table 7-3 gives a list of starting guesses for the single free parameter in the case of the constant temperature fitting.

Serial No.	c_1
1	800
2	650
3	500
4	350

Table 7-3: List of initial guesses for constant temperature profile

Fig 7-4 indicates that the axial temperature profile predicted using a uniform temperature profile across the channel does not depend on the initial guess for c_1 except for a two points in the pre-flame region where the CO_2 concentration is very low and therefore the uncertainty in the measurements is very high.

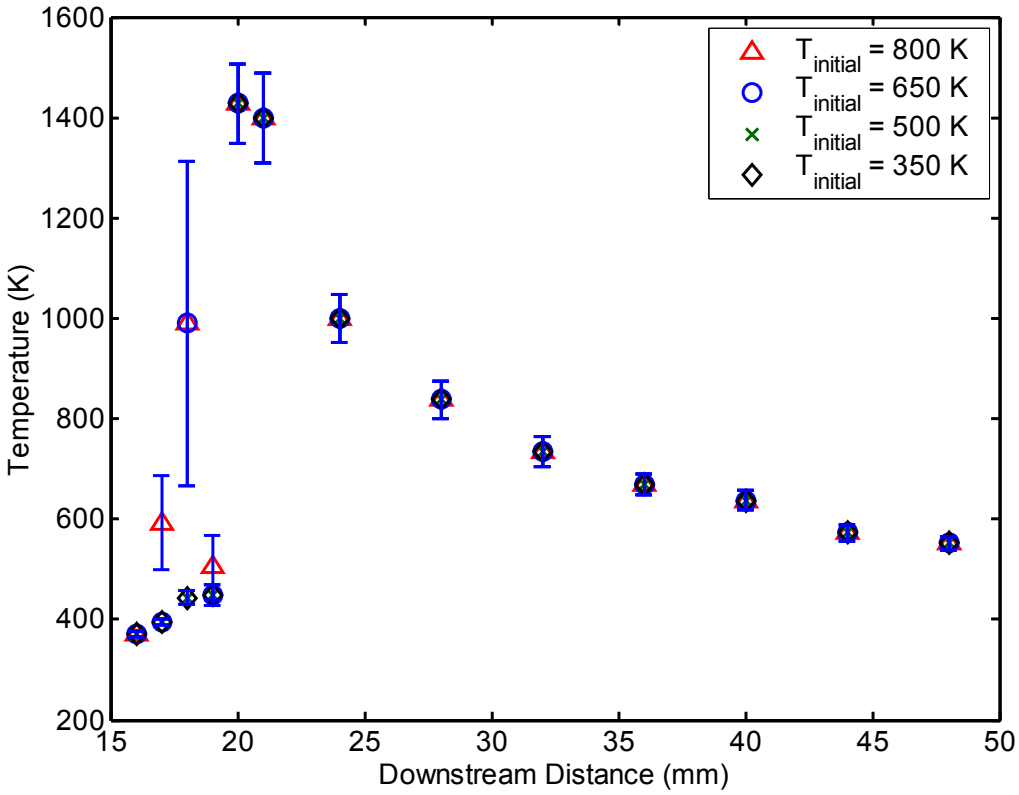

Figure 7-4: Comparison of peak axial temperature profiles for different initial guesses (constant temperature profile)

However, these points (650K, blue circles and 800K, red triangles) are readily identifiable as they correspond to situations where a converged solution was not obtained. This was either because the maximum number of iterations was reached with no convergence or a math overflow error occurred. This could be due to the fact that the initial guess is too far from the final solution (predicted from the other two guesses that did converge properly). The larger uncertainty associated with these points also helps identify points with potential convergence problems. Taken together, however, the results show that the convergence is unique as long as the initial guess is 'reasonable'.

b) 2^{nd} Order Fit:

The same test for unique convergence is applied to the 2^{nd} order polynomial temperature profile except that guesses for two free parameters, a_2 and c_2, are supplied. These guesses are listed in Table 7-4.

Set	a_2 (K/cm^2)	c_2 (K)
1	5e3	500
2	3e3	500
3	5e3	350
4	5e3	650
5	1e4	500
6	1e4	350

Table 7-4: List of initial guesses for 2^{nd} order temperature profile

Fig. 7-5 shows the peak axial temperature profiles predicted for the first 4 sets of guesses. The remaining two sets were not included in order to make the figure clearer. As can be seen from the figure the first 3 sets converge to the same values indicating the presence of a unique solution. In the fourth and subsequent sets, however, convergence problems like those described previously were experienced. This reinforces our earlier conclusion that the optimization routine converges to unique solutions as long as the initial guesses for the values of the temperature are not too far off.

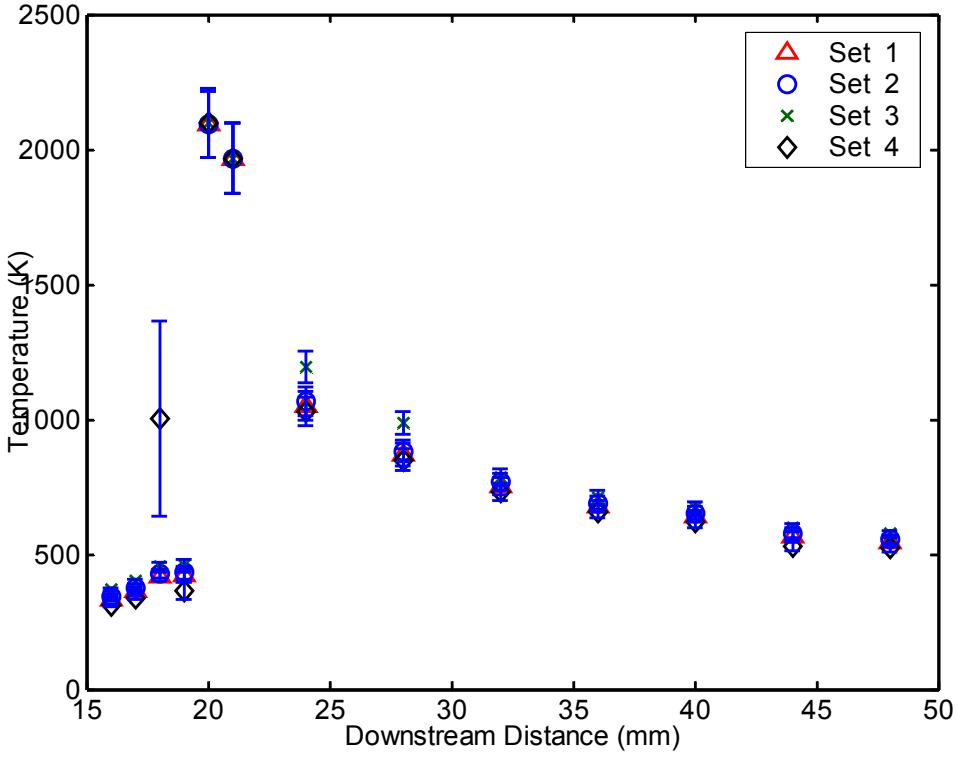

Figure 7-5: Comparison of peak axial temperature profiles for different initial guesses (2nd order temperature profile)

c) 4th Order Fit:

The same test for unique convergence is applied to the 4th order polynomial temperature profile except that guesses for three free parameters, c_4, d_4 and e_4, are supplied. These guesses are listed in Table 7-5.

Set	c_4 (K/cm^2)	d_4 (K/cm)	e_4 (K)
1	1e4	1e3	500
2	1e4	2e3	500
3	1e4	1e3	350
4	1e4	1e3	650
5	5e4	-1e3	500
6	1e4	1e3	500
7	1e4	-1e3	650
8	1e4	1e3	800

Table 7-5: List of initial guesses for 4th order temperature profile

Fig. 7-6 shows the plots of the peak temperature for the first 4 sets of guesses. As with the second order polynomial, the first 3 sets of initial guesses seem to be convergent but sets 4 and higher have convergence problems.

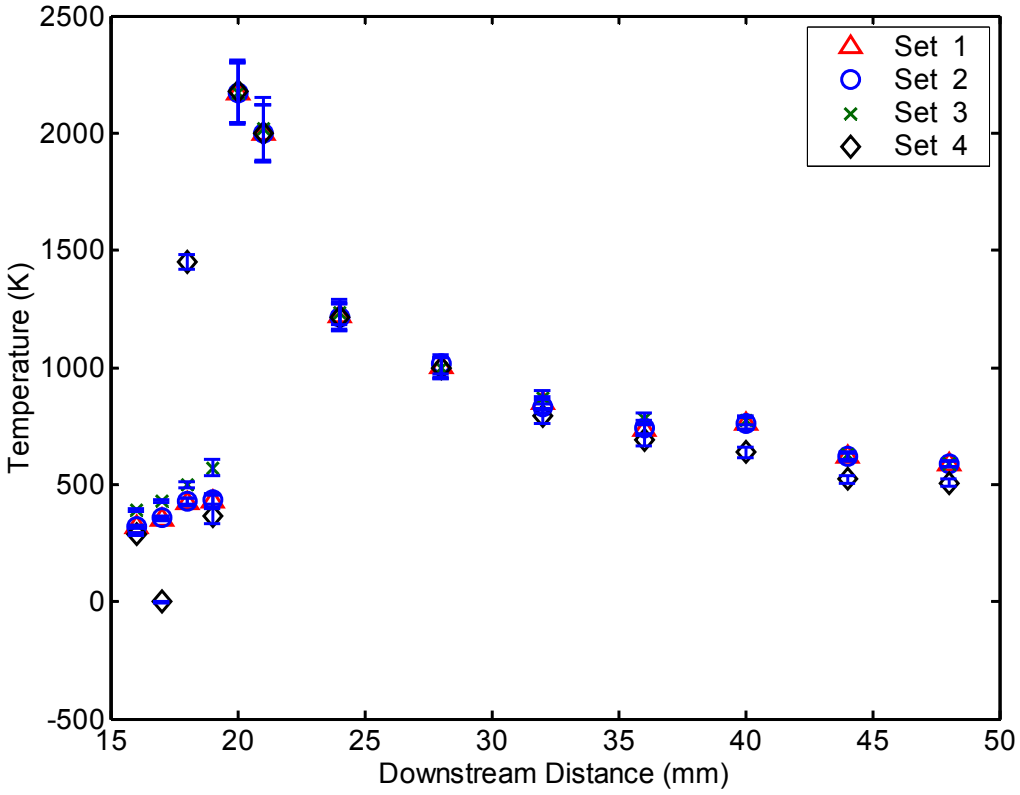

Figure 7-6: Comparison of peak axial temperature profiles for different initial guesses (4^{th} order temperature profile)

d) Comparison of different fits:

Fig. 7-7 compares the axial temperature profiles computed assuming uniform, 2^{nd} order, and 4^{th} order temperature profiles. It shows that the constant temperature fit and 2^{nd} order fit are consistent within their uncertainty limits in the pre and post-flame regions while the constant temperature profile leads to lower (and physically unrealistic) temperatures.

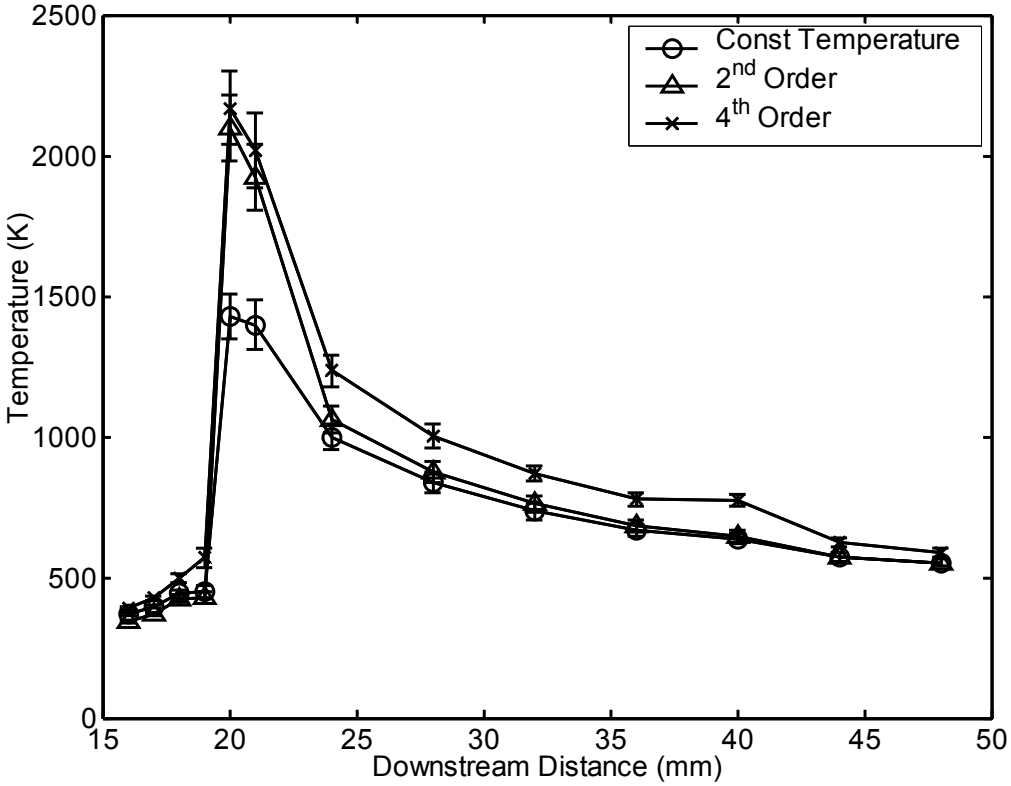

Figure 7-7: Comparison of peak axial temperature profiles for the three different functional forms of the cross-stream temperature profile.

Also, Figure 7-7 also demonstrates that the functional form of the temperature profile across the channel has a significant influence on the 'measured' temperature. This influence is not accounted for in the error bars presented in the figure.

7.2. Surface Temperature Measurements:

As indicated in Chapter 3, the outer surface temperature of the silicon plates is measured using an infrared camera. Fig. 7-8 is an uncorrected image of the temperature distribution in one of the silicon plates where the bright horizontal band corresponds to the location of the flame stabilized between the plates. The image

shows that the temperature distribution is quite uniform in the span wise direction indicating that the flow between the plates is mostly two-dimensional.

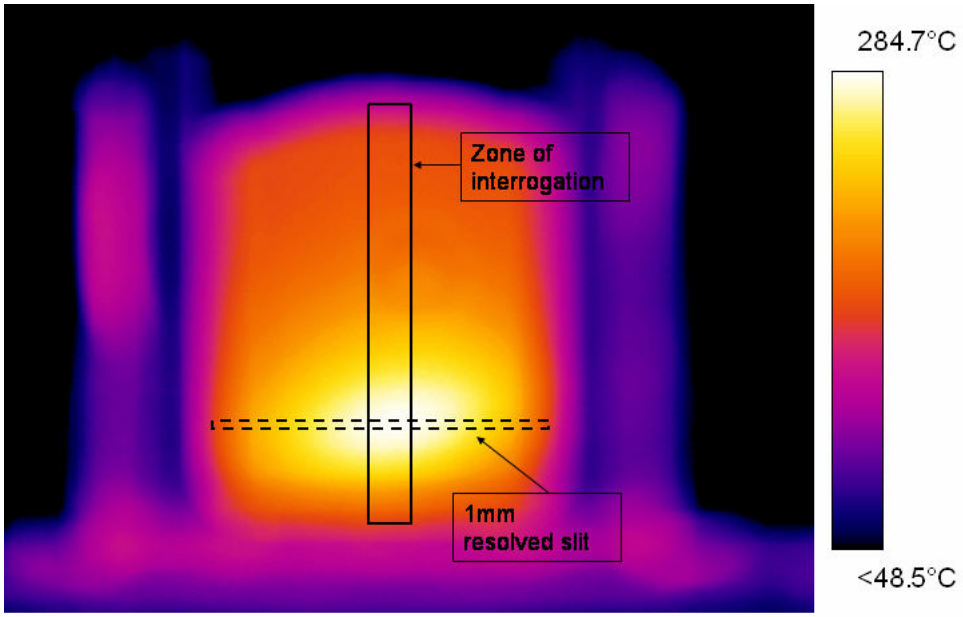

Figure 7-8: Infrared image of the outer surface (plate) of the combustor along with the interrogation region of the FTIR beam shown by the solid black box. The dashed black box shows the slit used for making measurements using the FTIR at a representative vertical position. $\phi = 0.86$, U = 44 cm/s, 2.15 mm wafer spacing.

Fig.7-9 compares the stream-wise evolution of the temperature of the outside surface of the plate to the centerline and near-wall gas temperatures predicted assuming that the gas temperature profile can be represented by a 2nd order profile. It shows that the centerline gas temperature peaks about 20 mm downstream of the

flashback arrestor and decreases with downstream distance as heat is lost to the walls.

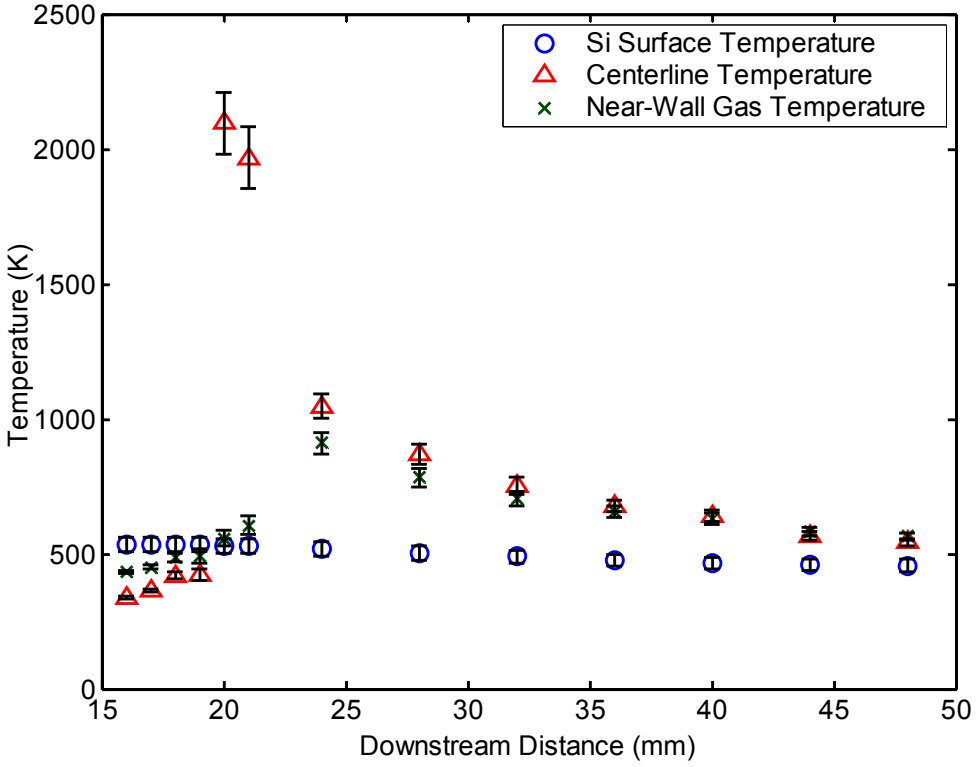

Figure 7-9: Axial variation of centerline gas (T_{ad} = 2093 K), wall gas, and surface temperatures corresponding to the boxed region in figure 7-8 for a 2nd order fit. The wafer spacing is 2.15 mm wafer spacing, ϕ = 0.86, and U = 44 cm/s.

The temperature of the gas near the wall and the outside temperature of the wall both show similar trends although the streamwise variation of the wall temperature is much smaller because the Biot number of the structure is so small (<0.01). It is also interesting to note that the outer wall temperature doesn't appear to change by much in the stream wise direction. A similar plot of gas temperatures is made for the 4th order fit in Fig. 7-10

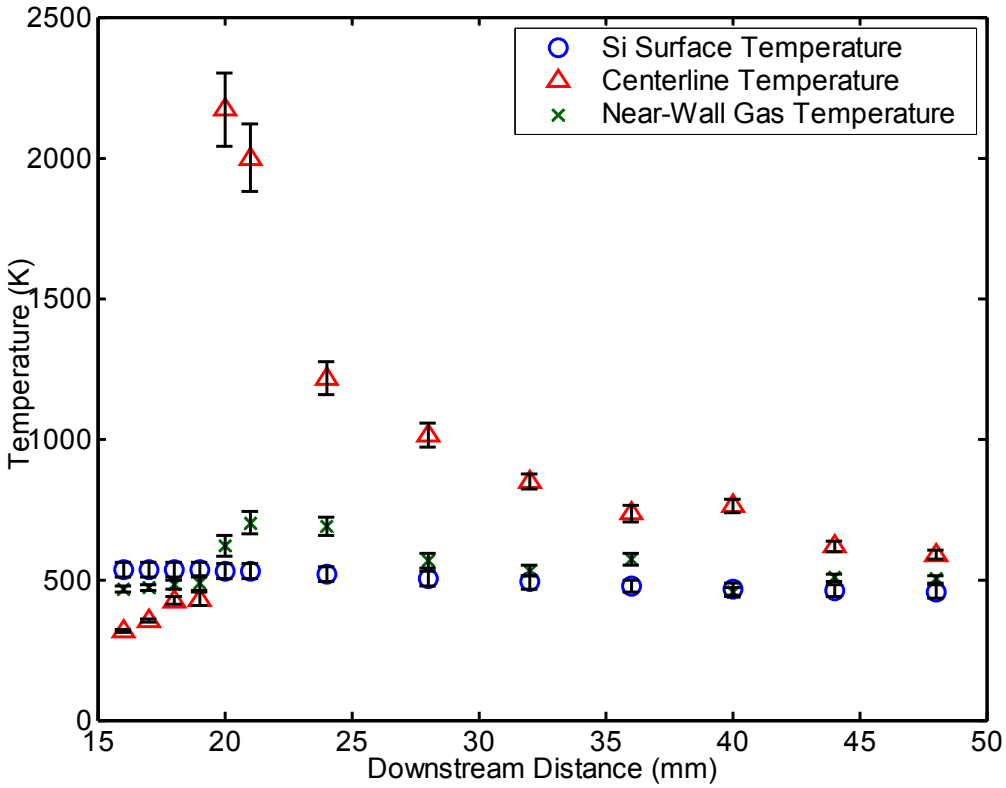

Figure 7-10: Axial variation of centerline gas (T_{ad} = 2093 K), wall gas, and surface temperatures corresponding to the boxed region in figure 7-8 for a 4th order fit. The wafer spacing is 2.15 mm wafer spacing, ϕ = 0.86, and U = 44 cm/s.

As can be seen the inner wall gas temperature seems to be closer to the outer wall temperature for this temperature profile than the 2nd order temperature profile.

7. 3. Overall 2D Picture:

The technique developed in this work, i.e., making line of sight temperature measurements by using a reasonable functional form for the temperature profile can

be taken one step further to make a full 2D picture of the temperature distribution in the channel. Fig. 7-11 shows the over all 2D temperature image for the 2nd order fit.

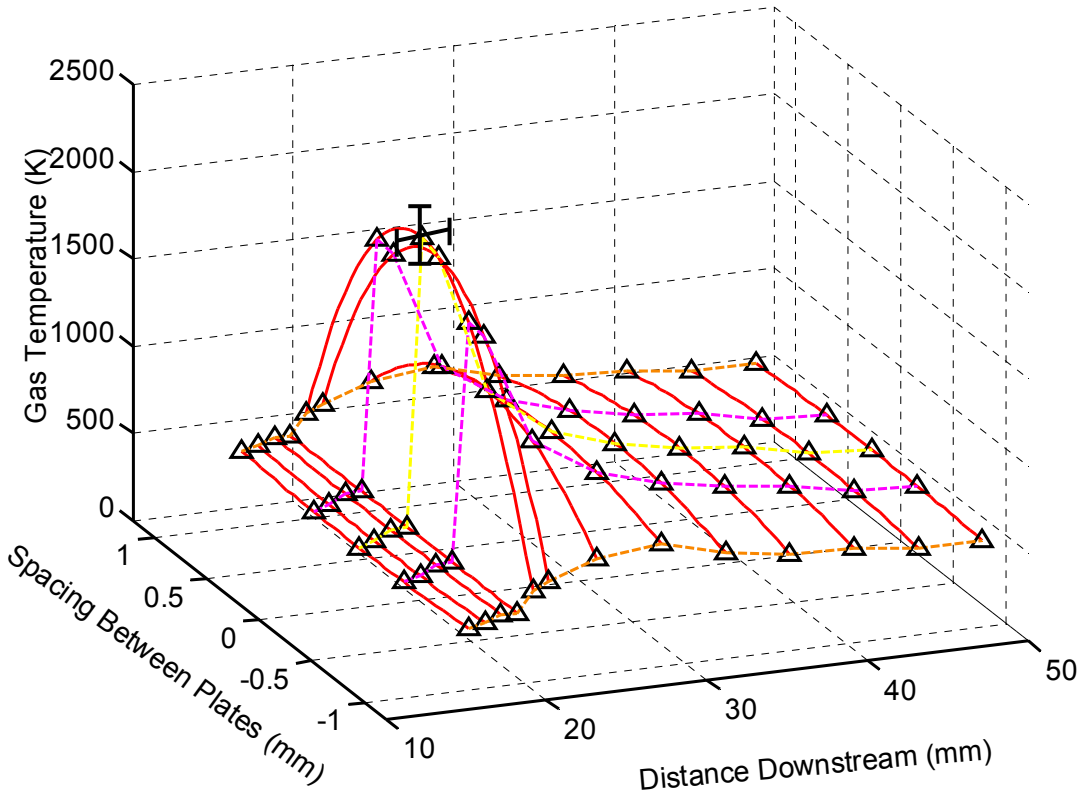

Figure 7-11: Overall 2D measured temperature profiles in the channel

Fig. 7-11 shows that the axial temperature profiles at different lateral locations all have the same overall trend as might be expected. The dashed lines in orange represent the near wall gas temperature. It is important to note that while CFD and simple modeling might yield complete profiles as represented in this figure experimental results of the same might be much harder to come by. The power of the non-intrusive diagnostic technique in making this line of sight temperature measurements in 2D is sufficiently well illustrated by this plot.

Fig. 7-11 has one drawback however, in that the high temperature value at the flame dominates the profiles and prevents the nature of the profiles at the pre-flame and post-flame from being distinguished clearly. Fig. 7-12 is a blow up of the pre-flame region profiles.

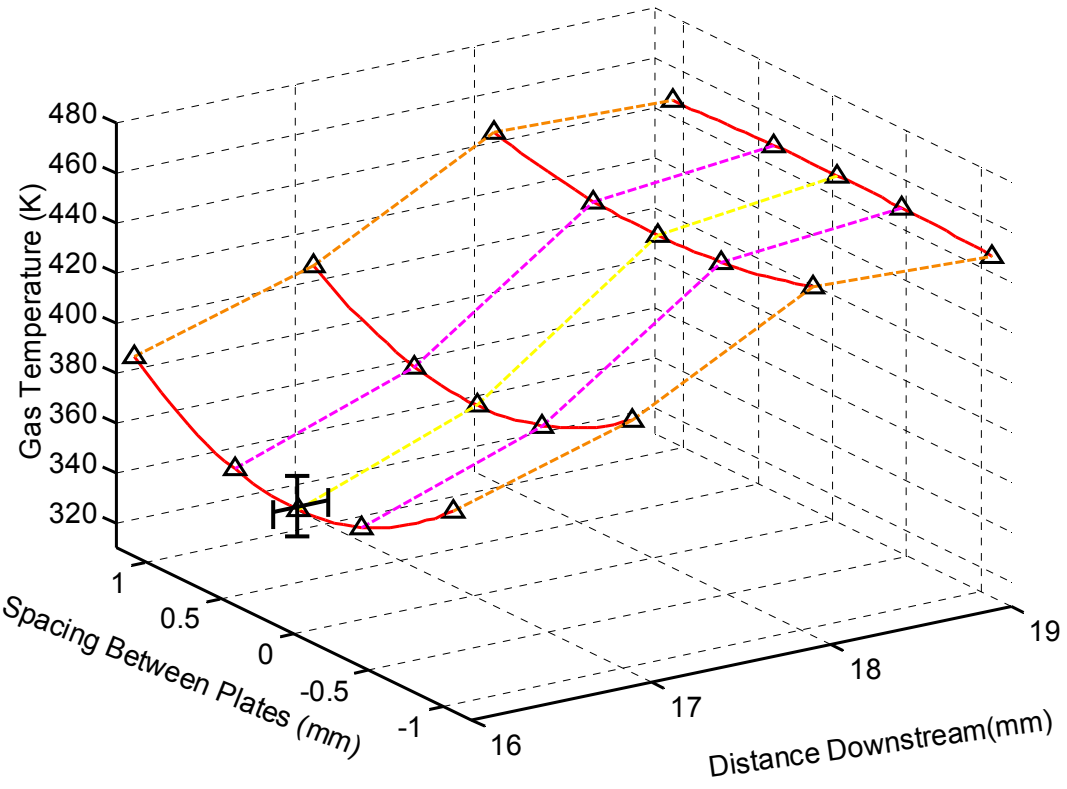

Figure 7-12: 2D temperature distribution in the pre-flame region

As can be seen from Fig. 7-12 the slope at the wall in the pre-flame will cause heat fluxes to flow from the wall to the gas (i.e. pre-heating of reactants owing to conduction of heat via the structure) which has also been predicted by models in past research (e.g. Leach *et al.*)

Like wise Fig. 7-13 is a blow up of the post flame region of the flame. The curvature of the temperature profile at the wall in the post-flame region indicates that the heat fluxes are flowing from the gas to the wall.

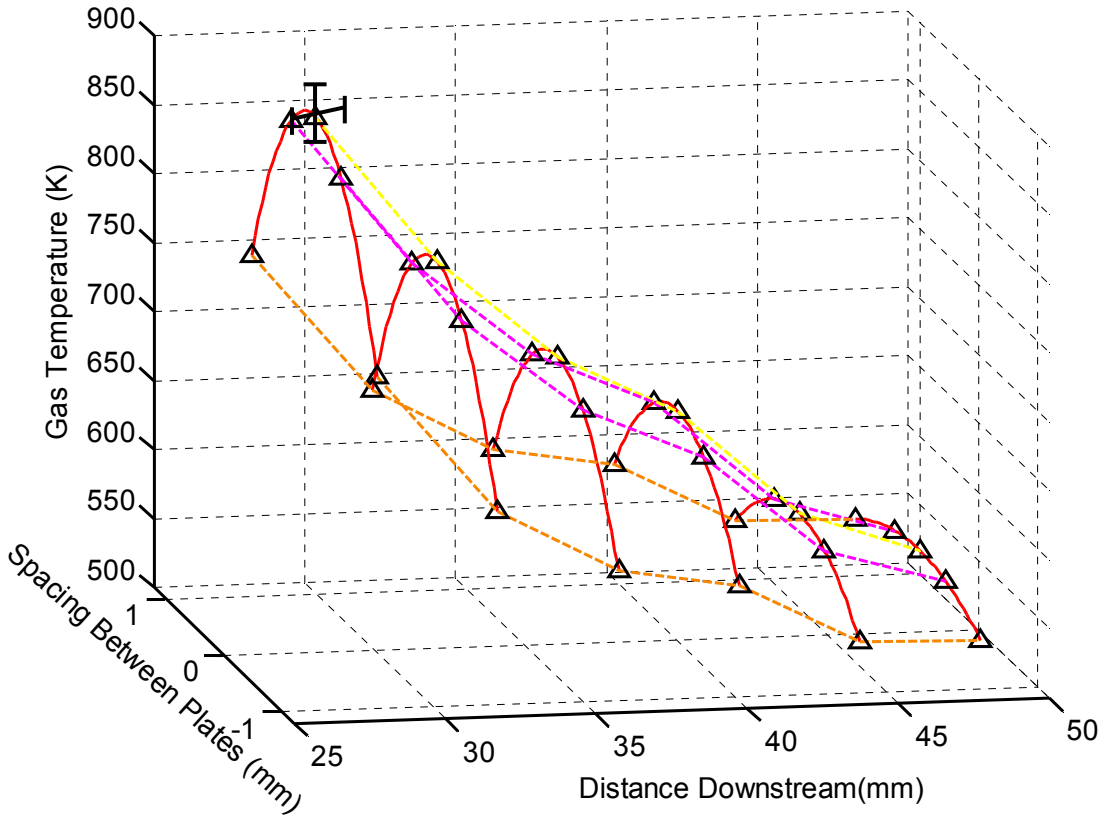

Figure 7-13: 2D temperature distribution in the post-flame region

7. 5. Energy balance validation:

The streamwise evolution of the gas temperature profiles near the wall and the outside temperature of the wall can also be used to estimate the streamwise evolution of the heat loss from the flame. The heat flux from the outer surface of the plate to

the environment results from the combined effects of natural convection and radiation:

$$\dot{q}''_{plate}(x) = \dot{q}''_{free\,conv}(x) + \dot{q}''_{rad}(x) \tag{7-8}$$

where

$$\dot{q}''_{rad}(x) = \varepsilon(T_p)\sigma(T_p^4(x) - T_\infty^4) \tag{7-9}$$

and

$$\dot{q}''_{free\,conv}(x) = h(x)\,(T_p - T_\infty) \tag{7-10}$$

where

$$h(x) = \frac{Nu(x)\ k_{gas}}{x}$$
$$and \quad Nu(x) = 0.387\ Ra(x)^{\frac{1}{4}} \tag{7-11}$$
$$and\ Ra(x) = \frac{g\beta(T_p - T_\infty)x^3}{\nu^2}\Pr$$

In these expressions, $T_p(x)$ is the outer surface temperature of the silicon plate at downstream location x, $\varepsilon(T_p)$ is the emissivity of silicon at T_p, T_∞ is the temperature of the environment, and σ is the Stephan-Boltzmann constant. The value of $\bar{h}$ corresponds to natural convection on a vertically oriented plate[52]. Fig. 7-14 shows a schematic diagram of the various heat fluxes when the μ-combustor is in operation.

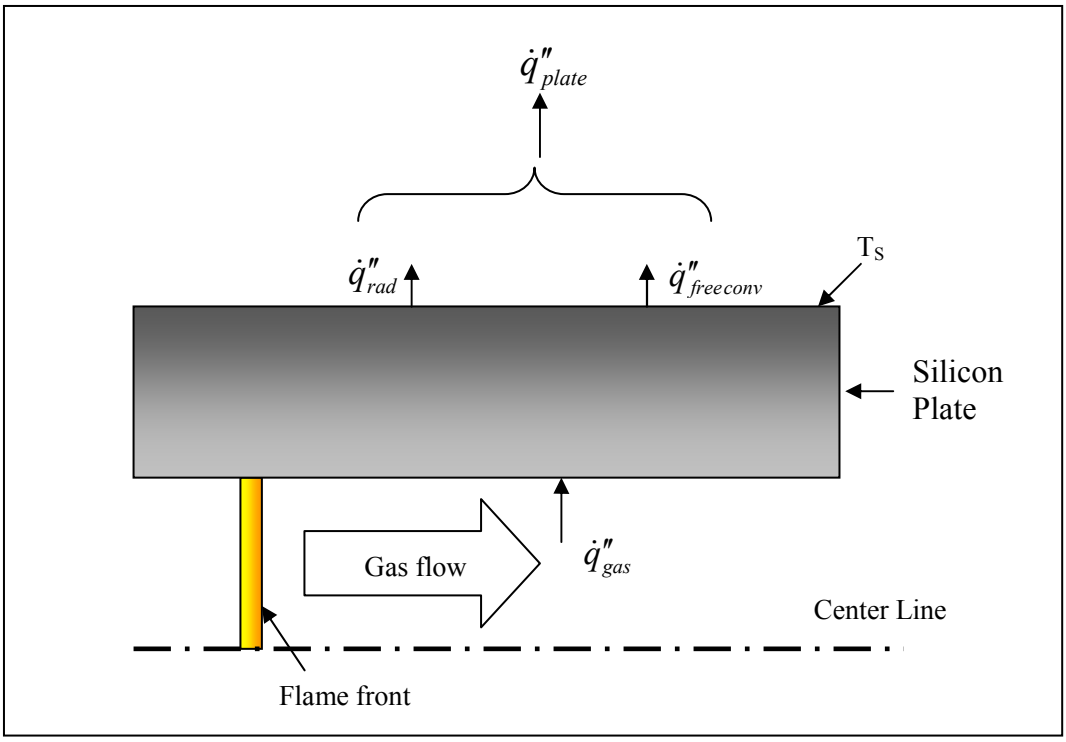

Figure 7-14: Schematic of heat transfer in the μ-combustor

The heat flux from the gas to the inner surface of the plate arises from the temperature gradient at the wall.

$$\dot{q}''_{gas} = -k_{gas}(T_w)\left.\frac{\partial T}{\partial y}\right|_{y=wall} \tag{7-12}$$

In this expression, k_{gas} is the thermal conductivity of the gas mixture (for which the value corresponding to N_2 is used) evaluated at the gas temperature at the wall T_w. The gas temperature at the wall and the temperature gradient at the wall are determined using the temperature profile (Eq. 7-2 for 2nd order fit) evaluated at $y = 0$. The results are presented in Fig. 7-15.

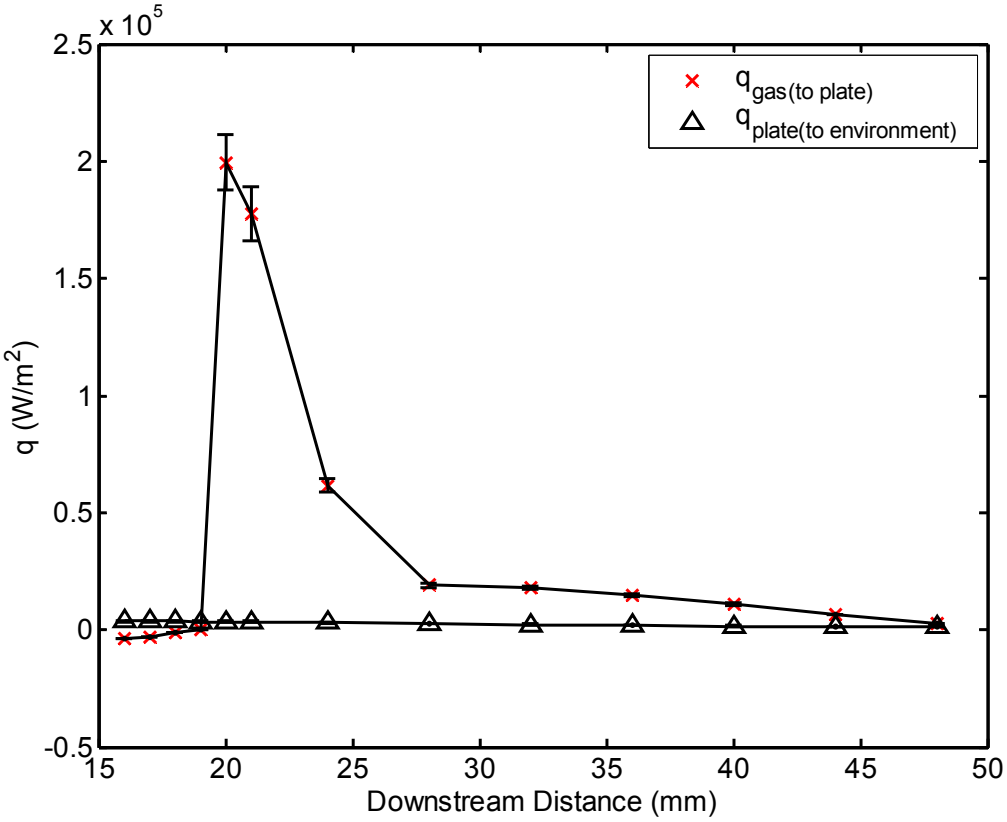

Figure 7-15: Comparison of heat fluxes (coming in to the plate from the hot gases and going out via radiation and convection)

They show that the heat loss is maximum in the immediate vicinity of the reaction zone and decreases as one moves downstream. The figure also shows that the heat flux from the hot gases to the inside of the silicon walls is significantly larger than that from the outside surface of the walls to the environment by radiation and convection. Integrating the gas to wall heat flux profile along the flow path gives a net heat loss per unit width of the plates of 2495.7 W/m. The corresponding heat production by the flame is approximately 2743.9 W/m, indicating that over 90% of the heat generated by the flame is transferred to the plates. Integrating the heat flux profile along the outer surface of the plate gives a heat flux of approximately 154 W/m from the plates to the environment, indicating that most of the heat that is

transferred to the plates is transported via conduction to regions of the burner structure that are not accounted for in the analysis.

An overall energy balance on the flow entering and exiting the interrogation region is performed in order to check that the relatively large rate of heat transfer to the structure predicted by the wall temperature profile is consistent with the gas temperature measured at the burner exit. This leads to the following expression for the gas temperature T_{out} leaving the interrogation region:

$$T_{out} = \frac{C_{p_i}}{C_{p_o}} T_{in} + \frac{\dot{m}_f h_R - \dot{Q}_p}{\dot{m} C_{p_o}} \tag{7-13}$$

In this expression, T_{in} is the temperature of the reactants entering the interrogation region, $\dot{m}$ is the mass flow rate of reactants, C_{p_i} and C_{p_o} are the specific heats of the reactants and products respectively, $\dot{m}_f$ is the mass flow rate of fuel, h_R, is the lower heating value of methane, and $\dot{Q}_p$ is the heat loss to the plates. Using Eq. (7-13) to compute T_{out} yields a gas temperature of 583 K which compares well, within the uncertainty of the measurement, to the average exit gas temperature of 568 K measured using the non-intrusive technique. As a result, the heat transfer measurements to the plate appear to be consistent with the gas temperature measurements and suggest – to first order at least – that the assumption of a 2nd order temperature distribution is reasonable. The large differences between the gas-to-wall and wall-to-environment heat fluxes indicate that most of the heat transferred to the combustor walls is transported (via conduction) to other parts of the combustor structure that are not accounted for in this calculation. How ever the important message to take from this calculation is that an energy balance based on heat

conduction to the plates from the gas (which in turn is based on the assumed functional form of the temperature profile) seems to confirm the validity of the measurements made.

7.6. Overall Heat Transfer Picture:

The calculations performed thus far can be used to build the overall picture of heat transfer in microcombustors such as the one used in this work. Fig. 7-16 is a sketch of the over all heat transfer picture.

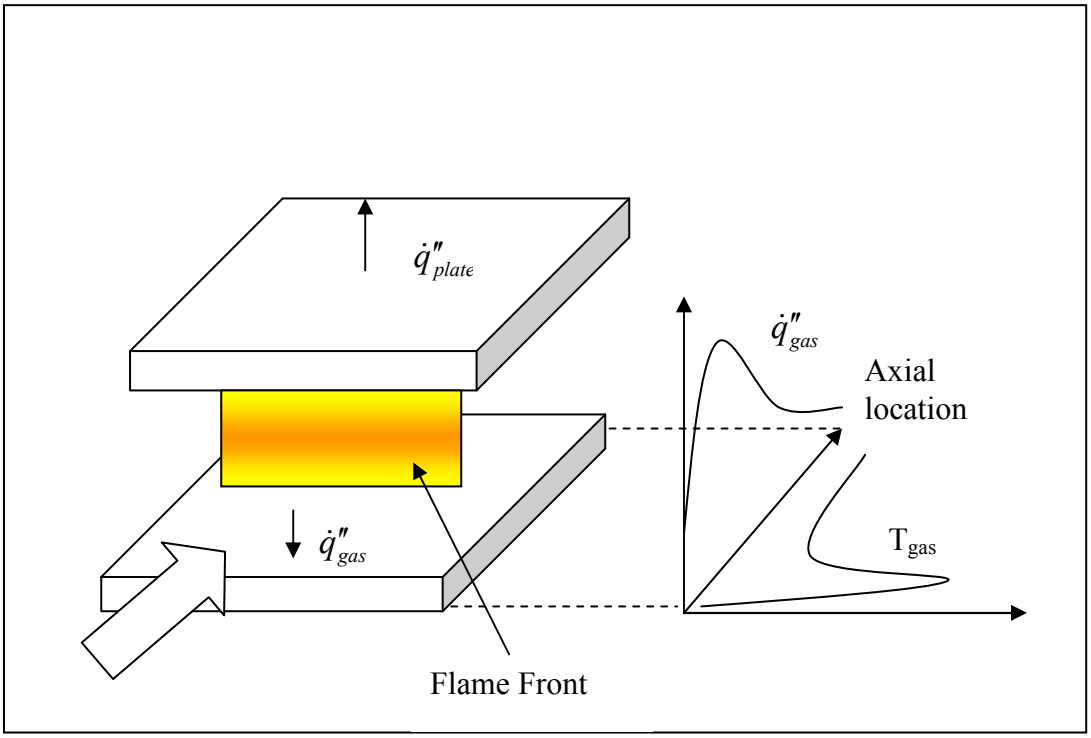

Figure 7-16: Schematic of over all heat transfer process in the μ-combustor

The sketch encapsulates the various results shown in this chapter thus far, the gas temperature profile along with the various heat fluxes.

Chapter 8: Conclusions and Future Work:

8.1. Key Contributions:

This thesis has investigated the heat transfer processes in microcombustors from theoretical and experimental points of view. A simple two dimensional theory has been developed based on the assumptions of slug flow and constant wall temperature for a parallel plate reactor with a combustion wave in it. The resulting energy equation was solved after non-dimensionalization leading to a solution for the non-dimensional temperature as a function of the spatial coordinates and the Peclet number. The asymptotic behavior of the solution was examined in the limits of large Peclet number and it was found that the two dimensional temperature approaches the solution for a one dimensional theory. Since Peclet number is directly proportional to flow velocity and channel width this may be interpreted as being due to the fact that if either the flow velocity is high or the channel width is large any thermal interaction between the wall and the gas flow will be localized and not penetrate the core of the flow. This results in the flow behaving as an adiabatic one dimensional flow in a thermal sense. At small Peclet numbers, the convective transport term is negligible compared to conductive terms and the mean temperature profile converges to the product a well known mathematical function known as the Lerch transcendent and an exponential.

The exact solution for the temperature profile across the channel is found to be a Fourier series expansion. The exact solution has also been used to obtain a Nusselt number correlation for heat transfer for flames propagating in infinitely long

parallel plate channels. Finally, using the exact solution it has been shown that the temperature profile can be represented using 2^{nd} and 4^{th} order polynomials that are symmetric about the channel center line. This fact is useful because it enables one to infer the temperature distribution along an optical line of sight from measurements of the integrated absorbance along that line of sight.

This new technique has been used to make measurements of transverse and longitudinal gas temperature distributions in a simulated micro-combustor with 1 mm spatial resolution in the flow direction using absorption from CO_2 produced naturally in the flame by "looking through" the silicon walls of the combustor. Gas temperatures in most regions of the flame can be determined within +/- 100K and are consistent with corrected thermocouple measurements. Accounting for the shape of the temperature distribution across the channel using 2^{nd} or 4^{th} order polynomials leads to heat fluxes that are consistent with an overall energy balance on the system. This diagnostic technique may prove useful in making performance measurements in future MEMS microcombustors. The results show that over 90% of the heat released in the flame is transferred to the walls while a much smaller fraction is lost to the environment. This indicates that the majority of the heat produced by the flame is transferred back to the incoming reactants or lost to other parts of the structure. This pre-heating of the reactants explains the increase in burning velocity observed in the burner and is consistent with theoretical investigations of flame stabilization in micro-combustors.

In summary, this thesis has developed a simple theory for heat transfer in a microcombustor and used it to determine the functional form for the gas temperature

distribution. This distribution has been used to make non-intrusive measurements of gas temperature and heat fluxes in a microcombustor. These measurements have enabled the first direct experimental measurements of heat recirculation in micro-combustors.

8.2. Future Work:

There are two things to be readily explored based on what has been observed in the work performed in this thesis. First, the simple heat transfer model needs to be improved to incorporate fully developed velocity profile to obtain similar solutions that can be used to check if fitting using polynomials work.

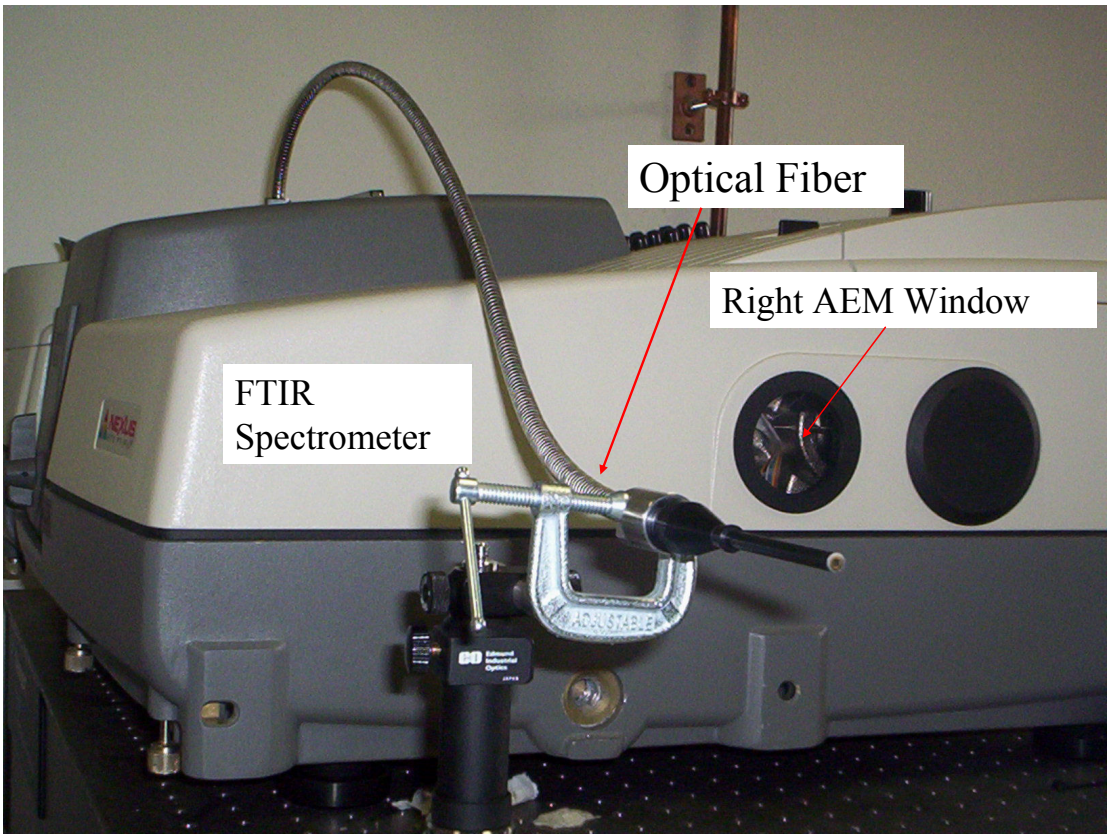

Figure 8-1: Photograph of fiber optic coupler

Second, the current experimental technique is limited by the framework of its external optics necessitating that any future experiments be built on an optical bench. An alternative to this might be to use a fiber optic coupler (shown in Fig. 8-1) which draws the IR beam directly from the sample compartment and sends it into a fiber optic cable which can be easily mounted on any desired experiment and any desired angle.

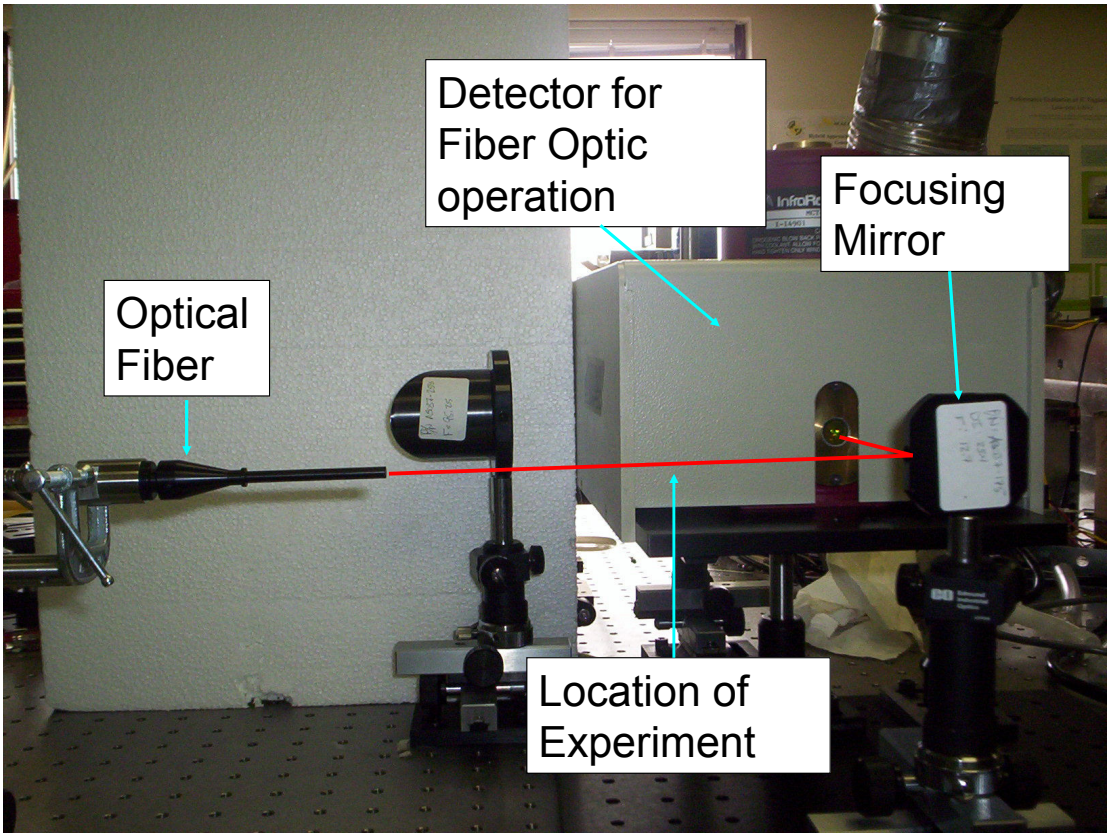

Figure 8-2: Beam path using the fiber optics

Fig. 8-2 shows the beam path while using the fiber optic cable. The fiber optic set up has its own external detector that is connected to the spectrometer and hence can be used in conjunction with a different experimental set up.

Appendix A:

Solution Procedure:

The partial differential equation to be solved is

$$Pe\frac{\partial\theta}{\partial x^{+}} = \frac{\partial^{2}\theta}{\partial x^{+2}} + \frac{\partial^{2}\theta}{\partial y^{+2}} \tag{A-1}$$

With boundary conditions

$$\begin{aligned}&\theta(-\infty, y^{+}) = 0;\\ &\theta(0, y^{+}) = 1; \quad \text{and} \quad \left.\frac{\partial\theta}{\partial y^{+}}\right|_{y^{+}=0} = 0 \quad \& \quad \theta(x^{+},1) = 0;\\ &\theta(\infty, y^{+}) = 0;\end{aligned} \tag{A-2}$$

Let

$$\theta(x^{+}, y^{+}) = X(x^{+})\, Y(y^{+}) \tag{A-3}$$

Substituting in the PDE and rearranging gives

$$\frac{-(X'' - Pe\, X')}{X} = \frac{Y''}{Y} = C \tag{A-4}$$

now if C equals zero. Then the solution for Y becomes

$$Y(y^{+}) = A\, y^{+} + B \tag{A-5}$$

Which on application of boundary condition gives trivial solution for Y and hence θ. Likewise if C were positive (equal to $+k^2$ say) the solution for Y becomes

$$Y(y^{+}) = A\, exp(k\, y^{+}) + B\, exp(-k\, y^{+}) \tag{A-6}$$

Again application of boundary conditions make both coefficients vanish and this leads to a trivial solution. Therefore the only admissible value for the constant is a negative number ($-\lambda^2$) and this then gives solutions for $Y(y^{+})$ as

$$Y(y^{+}) = A\cos(\lambda\, y^{+}) + B\sin(\lambda\, y^{+})$$

Application of the axisymmetric boundary condition shows that B must equal zero and application of the boundary condition at the wall shows that

$$\cos(\lambda) = 0 \qquad \text{i.e.} \qquad \lambda_n = \frac{(2n+1)\pi}{2} \tag{A-7}$$

Where λ_n are the eigen values for the equation. For this choice of a negative constant the equation for X is

$$X'' - Pe\,X' - \lambda_n^2\,X = 0 \tag{A-8}$$

Which has a solution of the form

$$X(x^+) = A_n \exp\left(\frac{Pe + \sqrt{Pe^2 + 4\lambda_n^2}}{2}\,\mathrm{x}^+\right) + B_n \exp\left(\frac{Pe - \sqrt{Pe^2 + 4\lambda_n^2}}{2}\,\mathrm{x}^+\right) \tag{A-9}$$

Clearly the boundary conditions at plus and minus infinity show that B_n is zero in the pre-flame region and that A_n is zero in the post-flame region. Thus the final solution comes out to be as presented in Chapter 2.

Bibliography

1. A. F. Bicen, D.G.N. Tse and J. H. Whitelaw, “Combustion characteristics of a model can type combustor”, *Combustion and Flame*, 1990, **80**, pp. 111-125.
2. W. P. Shih, J. G. Lee and D. A. Santavicca, “Stability and Emission Characteristics of a Lean Premixed Gas Turbine Combustor”, *Proceedings of the Combustion Institute*, 1996, **26**, pp. 2771-2778.
3. Jacquot, O. and P. Herve, “Determination of temperature fields in exhaust gases by infrared spectroscopy”, *Proceedings of SPIE*, 1998. **3493**, pp. 71-78.
4. D. Bailly, C. Camy-Peyret, and R. Lanquetin, “Temperature Measurements in Flames through CO_2 and CO Emission: New Highly Excited Levels of CO_2”, *Journal of Molecular Spectroscopy*, 1997, **182**, pp. 10-17.
5. J. S. Lindner, Z. Hansheng, and R. L. Cook, “Non-intrusive Determination of Combustion Efficiency Using FTIR Spectroscopy”, *Proceedings of SPIE*, 1995, **2365**, pp. 285-301.
6. C. P. Koshland, D. Lucas, B. S. Higgins, and R. F. Sawyer, “Detection of Chlorinated Hydrocarbons in Combustion Using In-Situ FTIR Spectroscopy”, *Proceedings of the Combustion Institute*, 1992, 24, pp. 1597-1604.
7. Ya. B Zeldovich, "Theory of Limit of Quiet Flame Propagation," *Zh.Prikl.Mekh.Tekh.Fiz*., 1941, **11** (1), pp. 159-169.
8. J. Daou and M. Matalon, “Influence of Conductive Heat-Losses on the Propagation of Premixed Flames in Channels”, *Combustion and Flame*, 2002, **128**, pp. 321- 339.

9. P. D. Ronney, “Analysis of non-adiabatic heat-recirculating combustors”, *Combustion and Flame*, 2003, **135**, pp. 421-439.

10. C. Cui, M. Matalon, J. Daou and J. Dold, “Effects of differential diffusion on thin and thick flames propagating in channels”, *Combustion Theory and Modeling*, 2004, **8**, pp. 41-64.

11. T. Leach and C. P. Cadou, “The Role of Structural Heat Exchange and Heat Loss in the Design of Efficient Silicon Micro-combustors”, Proceedings of the Combustion Institute, 2004, **30**, pp. 2437-2444.

12. T. Leach, C. Cadou, G. Jackson, “Effect of structural conduction and heat loss on combustion in micro-channels”, *Combustion Theory and Modelling*, 2006, **10** (1), pp. 85-103.

13. T. Takeno and K. Sato, “Excess Enthalpy Flame Theory”, *Combustion Science and Technology*, 1979, **20**, pp. 73-84.

14. T. Takeno, K. Sato and K. Hase, “A Theoretical Study on an Excess Enthalpy Flame”, *Proceedings of the Combustion Institute*, 1981, **18**, pp. 465-471.

15. Y. Kotani and T. Takeno, “An Experimental Study on Stability and Combustion Characteristics of an Excess Enthalpy Flame”, *Proceedings of the Combustion Institute*, 1982, **19**, pp. 1503-1509.

16. F. Weinberg, “Advanced Combustion Methods”, 1986, Orlando : Academic Press, Chapter 3.

17. A. Mehra, X. Zhang, A. A. Ayon, I. A. Waitz, M. A. Schmidt, and C. M. Spadaccini, “A Six-Wafer Combustion System for a Silicon Micro Gas Turbine Engine”, *Journal of MicroElectroMechanical Systems*, 2000, **9**(4), pp. 517-527.

18. A. Fernandez-Pello, "Micropower Generation Using Combustion: Issues and Approaches", *Proceedings of the Combustion Institute*, 2002, **29**, pp. 883-899.

19. H. T. Aichlmayr, D. B. Kittelson, and M. R. Zachariah, "Miniature free-piston homogeneous charge compression ignition engine-compressor concept- Part I: performance estimation and design considerations unique to small dimensions", *Chemical Engineering Science*, 2002, **57**, pp. 4161-4171.

20. H. T. Aichlmayr, D.B. Kittelson, and M.R. Zachariah, "Micro-HCCI combustion: experimental characterization and development of a detailed chemical kinetic model with coupled piston motion", *Combustion and Flame*, 2003, **135**, pp. 227-248.

21. P. D. Ronney, K. Takeda, K. Maruta, L. Sitzki, and K. Borer, "Catalytic Combustion in Microchannel for MEMS Power Generation", *The Third Asia-Pacific Conference on Combustion,* 2001.

22. P. D. Ronney, F. J. Weinberg, D. M. Rowe, and G. Min, "On Thermoelectric Power Conversion from Heat Recirculating Combustion Systems", *Proceedings of the Combustion Institute*, 2002, **29**, pp. 941-947.

23. W. J. A. Dahm, J. Ni, K. Mijit, J. R. Mayor, G. Qiao, S. W. Dyer, A. G. Benjamin, Y. Gu, Y. Lei, M. L. Papke, "Micro Internal Combustion Swing Engine (MICSE) for Portable Power Generation Systems". AIAA Paper 2002-0722, AIAA, Reno, NV (2002).

24. A. P. London, "Development and Test of a Microfabricated Bipropellant Rocket Engine", PhD dissertation, Massachusetts Institute of Technology, June 2000.

25. Graetz L., " Über die Wärmeleitus der fähigkeit von Flüssigkeiten," *Annalen der Physik and Chemie.*, 1883, **18**, pp. 79-94

26. J. R. Sellars, M. Tribus, J. S. Klein, "Heat Transfer to Laminar Flow in a Round Tube or Flat Conduit- The Graetz Problem Extended ", *Transactions of the ASME*, Feb 1956, pp. 441-448.

27. M. A. Ebadian and H. Y. Zhang, "An exact solution of extended Graetz problem with axial heat conduction", *International Journal of Heat and Mass Transfer*, 1989, **32** (9), pp. 1709-1717.

28. M. L. Michelsen and J. Villadsen, "The Graetz Problem with Axial Heat Conduction", *International Journal of Heat and Mass Transfer*, 1974, **17**, pp. 1391-1402.

29. A. S. Telles , E.M. Queiroz and G. ElmoÃ r Filho, "Solutions of the extended Graetz problem", *International Journal of Heat and Mass Transfer*, 2001, **44**, pp. 471-483.

30. J. Lahjomri and A. Oubarra, "Analytical Solution of the Graetz Problem with Axial Conduction", *Transactions of the ASME*, 1999, **121**, pp.1078-1083.

31. S. Kakac and Y.Yener, "Convective Heat Transfer", 2nd ed. 1995, CRC Press, pp. 132-180.

32. J. Jarosinksi, "Heat transfer between hot combustion gases and a cold wall in narrow channels for limit flames", *International Journal of Heat and Mass Transfer*, Technical Notes, 1984, **27** (7), pp. 1113-1116.

33. X. Yin and H. H. Bau, " The conjugate Graetz problem with axial conduction", *Transactions of the ASME*, 1996, **118**, pp. 482-484.

34. G. Maranzana, I. Perry, D. Maillet, "Mini- and micro-channels: influence of axial conduction in the walls", *International Journal of Heat and Mass Transfer*, 2004, **47**, pp. 3993- 4004.

35. C. Hsu, "An Exact Analysis of Low Peclet Number Thermal Entry Region Heat Transfer in Transversely NonuniformVelocity Fields", *Amerincan Institute of Chemical Engineers Journal*, 1971, **17** (3), pp. 732- 740.

36. J. Sucec and D. Radley, "Unsteady forced convection heat transfer in a channel", *International Journal of Heat and Mass Transfer*, 1990, **33** (4), pp. 683-690.

37. J. B. Campos Silva, R. M. Cotta, J. B. Aparecido. , "Analytical Solutions to simultaneously developing laminar flow inside parallel-plate channels", *International Journal of Heat and Mass Transfer*, 1992, **35** (4), pp. 887-895.

38. D. A. Nield, A.V. Kuznetsov and Ming Xiong, "Thermally developing forced convection in a porous medium: parallel plate channel with walls at uniform temperature, with axial conduction and viscous dissipation effects", *International Journal of Heat and Mass Transfer*, 2003, **46**, pp. 643-651.

39. S. T. Werely and L. Gui, "Advanced algorithms for microscale particle image velocimetry", *AIAA Journal*, 2002, **40**, pp. 1047-1055.

40. M. F. Modest and S. P. Bharadwaj, "Medium Resolution Transmission Measurements of CO_2 at High Temperature", *Journal of Quantitative Spectroscopy and Radiative Transfer*, 2002, **73** (2-5), pp.329-338.

41. L.S. Rothman, and et al., "The HITRAN Molecular Spectroscopic Database and HAWKS (HITRAN Atmospheric Workstation)", 1996 Edition.

42. Heland, J., K. Schafer, and R. Haus, *Investigations of Hot Exhaust Gases with Passive FTIR Emission Spectroscopy.* Proceedings of SPIE, 1998. **3493**: p. 2-10.

43. W. Grosshandler, "RADCAL: A Narrow-Band Model for Radiation Calculations in Combustion Enviroment", NIST Technical Note 1402, 1993.

44. A. Soufani and J. Taine, "High Temperature Gas Radiative Property Parameters of Statistical Narrow-Band Model for H2O, CO2 and CO and Correlated K-model for H2O", *International Journal of Heat Transfer*, 1997, **40**(4), pp. 987-991.

45. X. Zhang, A. Mehra, A. A. Ayon, and I. A. Waitz, "Igniters and temperature sensors for a micro-scale combustion system", *Sensor and Actuators*, 2003, **103**, pp. 253-262.

46. K. Breuer, J. Bird, G. Han, A. Westin, K. Johan and Z. Cao, "Infrared Diagnostics for Measuring Fluid and Solid Motion Inside Silicon Microdevices", *Microscale Thermophysical Engineering*, 2004, **8**(2), pp. 169-182.

47. S. Heatwole, C. P. Cadou, and S. G. Buckley, "In situ Infrared Diagnostics in a Silicon-Walled Microscale Combustion Reactor: Initial Measurements", *Combustion Science and Technology*, 2005, **177**, pp. 1449-1461.

48. K. Maruta, J. K. Parc, K. C. Oh, T. Fujimori, S. S. Minaev, and R. V. Fursenko, "Characteristics of Microscale Combustion in a Narrow Heated Channel", *Combustion, Explosion and Shock Waves*, 2004, **40** (5), pp. 516-523.

49. F. A. Williams, "Combustion Theory", 2nd ed. 1985, Addison-Wesley Publishing Company, California, page 273.

50. W. A. Strauss, "Partial Differential Equations- An Introduction", 1992, John Wiley and Sons, Inc., page 129.

51. Gradshteyn, I. S. and Ryzhik, I. M. "The Lerch Function $\Phi(z, s, v)$." 2000, §9.55 in Tables of Integrals, Series, and Products, 6th ed. San Diego, CA: Academic Press, pp. 1029.

52. A. Bejan, "Convection heat transfer", 3rd ed. 2004, Wiley, New Jersey, Chapters 3 and 4.

53. J. S. Winn, "Physical Chemistry", 1995, HarperCollins College Publishers, New York, Chapters 18-20.

54. D. A. McQuarrie, "Quantum Chemistry", 1983, University Science Books, California, Chapter 10.

55. D. Harris, Exploring Chemical Analysis, 3rd edition, W.H. Freeman & Company, 2004.

56. W. Malkmus, "Random band Lorentz with exponential tailed 1/S line-intensity distribution function", *Journal of the Optical Society of America*, 1967, **57**, pp. 323-329.

57. NIST Database for Atomic Spectra, http://physics.nist.gov/PhysRefData/ASD/index.html

58. A. Pettersson, "Investigations of Infrared Chemiluminescence Emission from Laboratory Flames", M.S. thesis, Lund Institute of Technology, Lund University, 2004.

59. W.R. Runyan, "Technology Semiconductor Silicon", McGraw-Hill Book Company, 1996.